A PARAMETRIC STUDY OF DELAMINATIONS IN AN ALUMINUM-LITHIUM ALLOY

BY

SEAN FENNER HAMEL

THESIS

Submitted in partial fulfillment of the requirements
for the degree of Master of Science in Mechanical Engineering
in the Graduate College of the
University of Illinois at Urbana-Champaign, 2010

Urbana, Illinois

Adviser:

Professor Armand Beaudoin

Abstract

The significant advantages in weight reduction and increased strength have placed advanced aluminum-lithium alloys at the forefront of aerospace materials research. Delaminations in these alloys play a significant role in their fracture processes. Therefore, a more complete understanding of the factors that influence the behavior of these delaminations and their corresponding effect on the primary crack behavior is the motivation for this study. The effects of texturing from mechanical processing, and the varying fracture toughness from heat treatments are the focus of the current study.

An elasto-viscoplastic model, based on the mechanical threshold state variable, was adopted to describe the constitutive behavior of these alloys, and was incorporated into a small-scale yield bi-crystal finite element model. This finite element model was then enhanced by inserting cohesive zone elements into planes where cracks are expected. These specialized elements not only simulate the initiation of cracks, but dynamically illustrate their subsequent growth as well. This framework was used to conduct parametric studies on the effects of texturing and fracture toughness on the behavior of the primary crack and any delaminations that may form in the crack-divider configuration.

To my wife,
whose unending love and support
made this possible.

Acknowledgements

There were many people involved with my graduate studies and the preparation of this work that I am indebted to, but two have to be thanked before the rest. If it were not for my dearest wife Adria, my college career would have fizzled out before it even started. It was her support and encouragement that bore me through the hardest moments of this journey. For that I am eternally grateful. Second I would like to thank my advisor Armand Beaudoin for his guidance and patience throughout this process. The greatest lesson he taught me was that of responsibility for my work and to honestly explore the topics in which I had the greatest interest. For anyone that knows me, that was no easy feat. To these two individuals no amount of thanks could ever be enough.

I am especially thankful to have had the opportunity to work with a fantastic research group. They were always there to lend a hand when I needed one. I would especially like to thank Dr. Russell McDonald who was my sounding board for pretty much everything. His was the brain I picked the most when I couldn't figure something out. His expertise on the characterization of delaminations in aluminum lithium alloys was an unending fountain of information. The collective works of Mark Hernquist and Wes Tayon were also pivotal to this work. They provided a plethora of experimental data that guided many of the decisions I made in the development of this work. Thanks to all of you.

Finally I would like to thank my family. My parents John and Kathleen taught me the importance of honesty in all endeavors and that loyalty to family and friends is the greatest virtue. I could not have had better role models growing up. My brother James has always had a talent for lightening my load through humor, which has always been greatly appreciated.

Table of Contents

List of Figures

List of Tables

1 Introduction and Motivation

Substantial improvements in structural efficiency, fuel savings, and payload capacities in aerospace applications can result if the net weight of a structure is reduced considerably. Weight reductions due to design modifications alone are marginal compared to what can be achieved through the use of materials with lower density. Each wt% addition of Lithium (Li), the lightest metallic element, to aluminum (Al) offers nearly a 3% reduction in density [1]. Moreover, Li enhances the elastic modulus of Al nearly 6% per unit weight % of Li addition. In addition to all of these benefits, Al-Li alloys have been found to exhibit superior mechanical properties at cryogenic temperatures as compared to conventional aluminum alloys [2]. It is no surprise that engineers in the aerospace industry are interested in using Al-Li alloys for critical components in their designs.

Despite the multiple advantages that aluminum-lithium alloys have over conventional aluminum alloys, there are disadvantages. In many aerospace applications, the material is rolled into sheets or wrought into complex shapes. These forming processes cause an anisotropic texture (a preferred set of crystal orientations), as well as high aspect ratio grain geometries. Figure 1.1 illustrates a micrograph of a portion of Al-Li rolled plate. The average grain sizes are approximately 1.2 x 0.9 x 0.09 mm in the L x T x S directions respectively (see figure 1.1 for definition of directions). This corresponds to an aspect ratio of roughly 14 [3]. As an example of chemical composition typical of Al-Li alloys consider 2099-T861 shown in table 1.1.

Table 1.1: Chemical composition of Aluminum-Lithium alloy 2099-T861 [4]

Comp	Cu	Li	Zn	Mg	Mn	Zr	Si	Fe	Ti	Al
wt%	2.58	1.73	0.6	0.26	0.25	0.09	0.03	0.03	0.01	Bal.

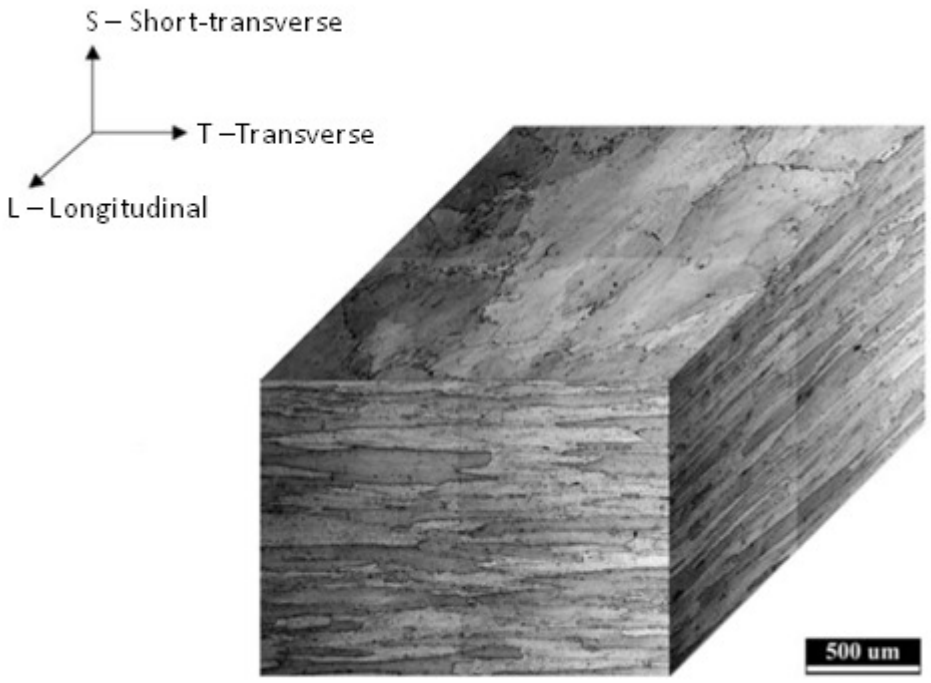

Figure1.1: Optical micrograph showing the microstructure at the edge of a rolled 2099-T861 plate [adapted from 3].

Depending on the alloying elements, Al-Li alloys show a wide variety of precipitates that are dispersed throughout the matrix or concentrated along grain boundaries. The location, size, density, and type of these precipitates affect the strength and ductility, as well as the localized deformations that Al-Li alloys are known for. Localized deformation refers to the tendency for a material to continue to deform on a specific slip plane rather than at a previously un-slipped location. Some of the most common precipitates are δ (AlLi), δ' (Al_3Li), T_1 (Al_2CuLi), θ' (Al_2Cu), and β' (Al_3Zr) [5].

The δ-phase nucleates during the quenching process near regions of high dislocation density that usually correspond to high angle grain boundaries where dislocations have difficulty moving into adjacent grains. Precipitation hardening of Al-Li alloys is known to be greatly influenced by the homogeneous dispersion of spherical δ' precipitates, which have a highly ordered structure [6]. During plastic flow, these particles are easily sheared by dislocations, which promote localization of slip along preferential crystallographic planes as well as serrated flow. This process is commonly

associated with the Portevin-LeChâtelier (PLC) effect and a negative strain-rate sensitivity. Researchers have observed that the T_1 and θ'-phases are concentrated at grain boundary interfaces and acts as impenetrable barriers for dislocation glide [5, 7, 8]. Finally, the perpetuity of the pancake like structure through heat treatment is due to the β'-phase that suppresses recrystallization [9]. The competition for alloying elements (Li and Cu) in the aforementioned precipitates can create precipitate free zones near grain boundaries that do not inhibit dislocation motion. In addition, there exists a multitude of other trace precipitates and tramp elements that may contribute to the delamination phenomenon [5].

Delamination of Al-Li alloys is similar to the failure mode of composite materials with the same name [10]. However, it is often related to the intergranular fracture along the longitudinal direction in the presence of plastic deformation caused by a growing primary crack. Three general types of delamination cracking have been classified, depending on the orientation of the primary crack with respect to the delamination plane (figure 1.2a-b) [11]. As a note to the reader, the convention used for orientation naming is the loading direction followed by the direction of primary crack growth. For example, T-S refers to loading a specimen in the transverse direction and propagation of the primary crack is in the short-transverse direction, also referred to as the crack arrester configuration.

The first configuration is known as the crack splitter (see figure 1.2b). The load is applied in the short-transverse direction, which is aligned with the elongated grains. A sample in this orientation fails in the traditional manner, but results in relatively low fracture toughness. This loss of fracture toughness is attributed to the weak grain interactions in the short transverse direction. When the loading direction is not aligned with the S direction, as is the case for the crack arrester and crack divider configurations, the primary crack grows in the customary direction with delamination cracks growing perpendicular to it. Both the crack divider and the crack arrester configurations typically show an apparent increase in fracture toughness. This is

because the growth of the primary crack is slowed by the out of plane delamination cracks that dissipate energy [5].

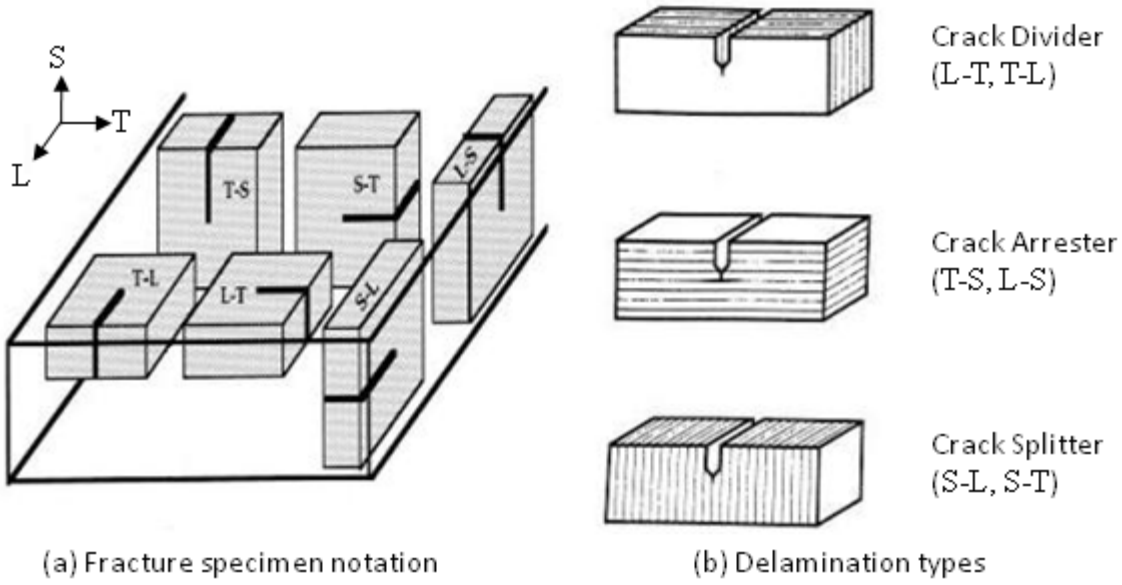

Figure 1.2: (a) Fracture specimen notation in rolled plate (L - Longitudinal direction, T - Transverse direction, S - Short-transverse direction) (b) Types of delaminations in fracture toughness specimens [adapted from 11]

Since delamination failure is associated with the separation of grain boundaries, the orientation of adjacent grains is very important to their interaction. A method to locally measure grain orientations near delaminations is Electron Back-Scatter Diffraction (EBSD). EBSD is a scanning electron microscope-based technique used to characterize microstructures and textures in crystalline materials. In EBSD, the SEM electron beam strikes an appropriately prepared sample surface at a high angle of incidence, optimally 70 degrees [12], as shown in figure 1.3a. This glancing angle allows most of the incident electrons to penetrate, scatter, and propagate from the surface with minimal energy loss. This minimization of energy loss is important because it produces a high resolution diffraction pattern like the one illustrated in figure 1.3b. This diffraction pattern is analyzed by an acquisition and indexing software to determine the position and orientation of diffraction bands, which allows an orientation map of the sample surface to be made [12].

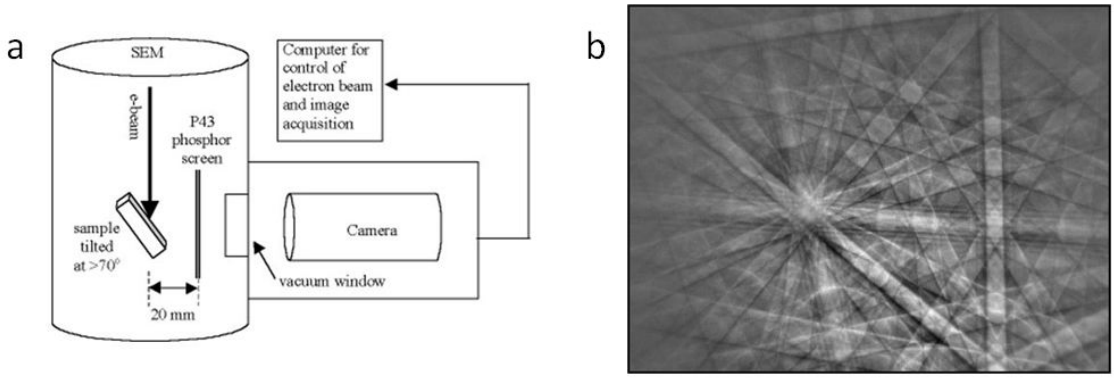

Figure 1.3: (a) Experimental setup of an EBSD analysis [13]. (b) Electron diffraction pattern produced by EBSD [12].

Studies done by various researchers, including Yoder [14], Tayon [15], and Hernquist [5], have made it clear that the prevalent orientations in Al-Li alloys are comprised of brass, copper, cube, and S (see Table 5.3). Figure 1.4 shows an EBSD orientation map of Al-Li 2195 from a middle tension (M(T)) sample. This figure illustrates the prevalence of the aforementioned orientations. An M(T) specimen was analyzed after delamination to find which orientation pairs were most susceptible to delamination. Figure 1.5 shows the EBSD orientation map of such a sample, and indicates that the brass and S pair tends to delaminate. This and similar data motivated the choices of simulated grain pairs, which will be described with more detail in subsequent chapters.

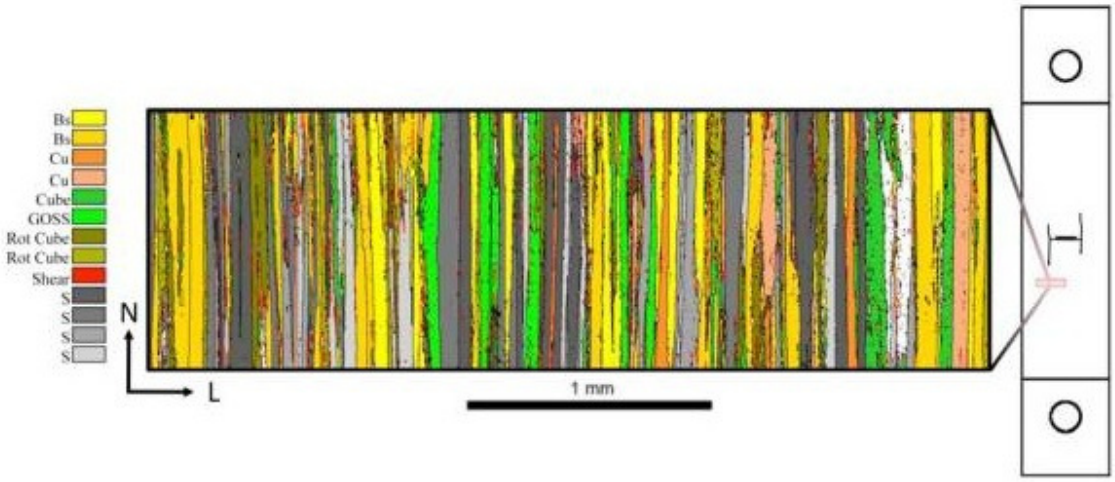

Figure 1.4: Preliminary EBSD scan to determine material texture in region of delaminations [5].

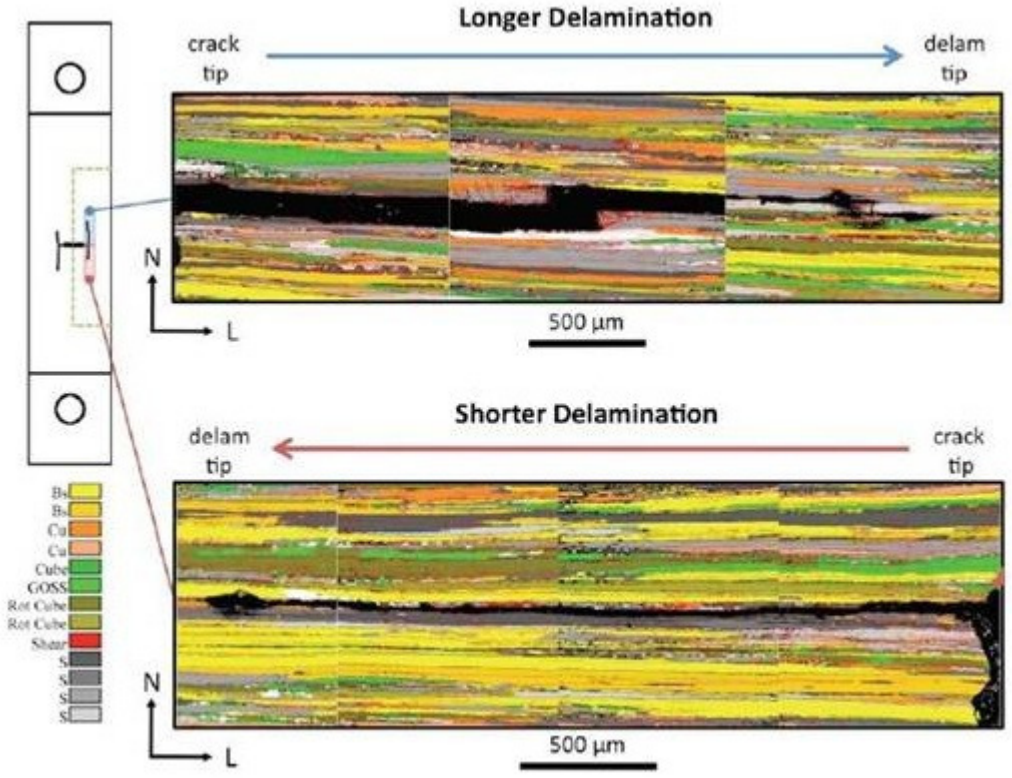

Figure 1.5: EBSD scans of delaminations in an M(T) specimen [5].

The recent advances in the development of Al-Li alloys for aerospace applications have created a variety of different processing procedures that produce highly textured alloys with a wide range fracture toughness values. This study aims at forming a better understanding of how texture and toughness affect the delamination process and, as a result, the behavior of the primary crack in the crack divider configuration. This manuscript begins with a description of a model that can be used to simulate the behavior of Al-Li alloys as well as the initiation and growth of both the primary crack and any delaminations. The simulation of the fracture process will be accomplished by embedding cohesive zone elements, the details of which are laid out in chapter 3, inside the aforementioned crystal plasticity model. A finite element code, based upon this formulation, was authored by Dr. Curtis Sam, using the framework developed by Dr. Satya Varadhan [16]. The mesh and boundary conditions, also developed by Dr. Sam, are outlined in Chapter 4. The present author applied this finite

element model to conduct a parametric study of the effect of grain interaction at the primary crack and delamination interface, detailed in Chapter 5. Trends noted in the parametric study are summarized in Chapter 6, along with recommendations for future work.

2 Material Modeling

In this chapter, the details of the model employed by this work are laid out. As with most metals in the large deformation setting, elastic strains are small but can have relatively large local plastic strains. To bridge all levels of strain, a multiplicative decomposition of the deformation gradient was utilized. This discussion will begin with a standard rate dependent Taylor model utilizing a power law relationship between stress and strain rate [17]. Then, Follansbee and Kocks' mechanical threshold stress (MTS) model is introduced to better capture rate dependence over a larger range of strains as well as introduce temperature dependence [18]. The discussion of kinematics and polycrystalline constitutive theory has been presented by numerous authors, therefore an in depth discussion will be unnecessary. However, for clarity, a summary of the theory will be presented below and is primarily based on the 2002 PhD Dissertation of Schalk Kok [19].

2.1 Kinematics

The deformation gradient ($\mathbf{F}$) given by

$$\mathbf{F} = \frac{d\underline{\mathbf{x}}}{d\underline{\mathbf{X}}} \quad , \tag{2.1}$$

is defined as the derivative of deformation in the current (Cauchy) frame ($\underline{\mathbf{x}}$) with respect to the reference (Lab) frame ($\underline{\mathbf{X}}$) [20]. In the discussion to follow, bold face type with no underline represents second order tensor quantities, while bold face type with a single underline represents vector quantities.

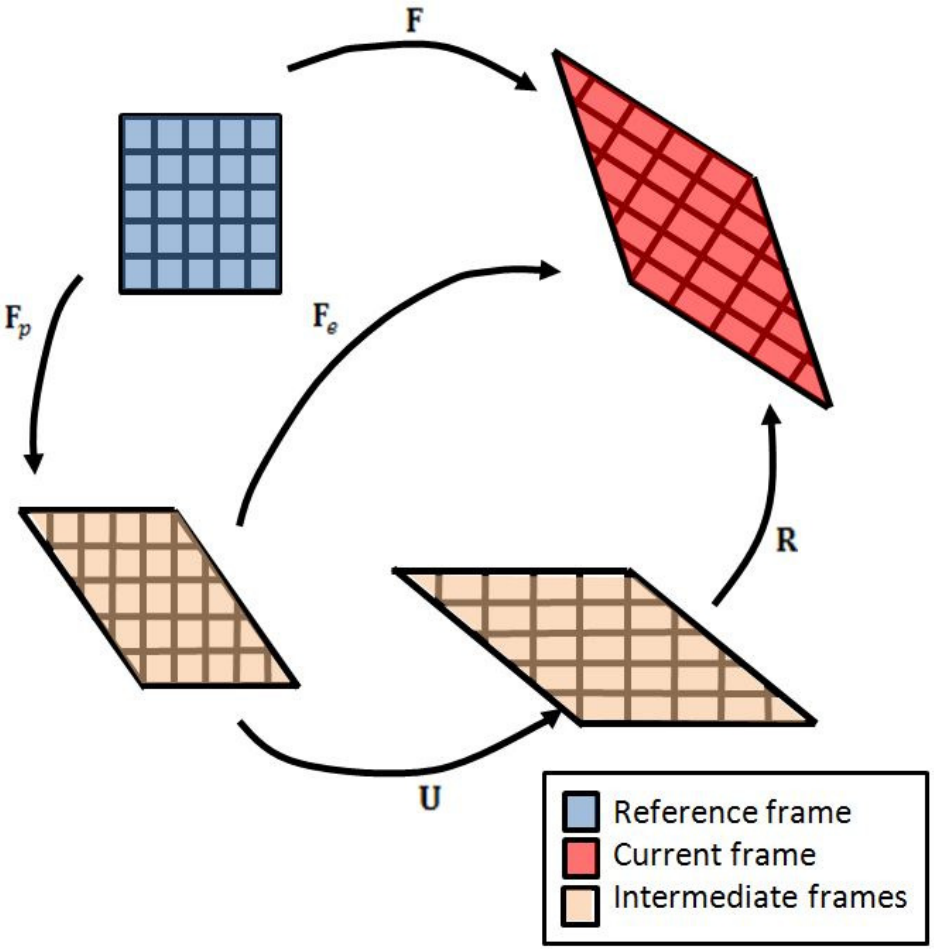

Figure 2.1: Multiplicative decomposition of the deformation gradient $\mathbf{F} = \mathbf{RUF}_p$.

The behavior of a single crystal is based on the multiplicative decomposition of the deformation gradient $\mathbf{F}$ into elastic $(\mathbf{F}_e)$ and plastic $(\mathbf{F}_p)$ parts (figure 2). The plastic part is due entirely to the shearing of slip systems, and the elastic part is due to both lattice stretch $(\mathbf{U})$ and rotation $(\mathbf{R})$.

$$\mathbf{F} = \mathbf{F}_e\mathbf{F}_p = \mathbf{RUF}_p \tag{2.2}$$

The velocity gradient $(\mathbf{L})$ is related to the deformation gradient and the rate of the deformation gradient $(\dot{\mathbf{F}})$, by the usual definition [20]:

$$\mathbf{L} = \frac{d\underline{\dot{\mathbf{x}}}}{d\underline{\mathbf{x}}} = \frac{d\underline{\dot{\mathbf{x}}}}{d\underline{\mathbf{X}}}\frac{d\underline{\mathbf{X}}}{d\underline{\mathbf{x}}} = \dot{\mathbf{F}}\mathbf{F}^{-1} \quad , \tag{2.3}$$

where a dot represents the time derivative. Using Eq. 2.2 and 2.3, $\mathbf{L}$ can be expressed as

$$\mathbf{L} = \dot{\mathbf{R}}\mathbf{R}^{\mathrm{T}} + \mathbf{R}\dot{\mathbf{U}}\mathbf{U}^{-1}\mathbf{R}^{\mathrm{T}} + \mathbf{R}\mathbf{U}\mathbf{L}_p\mathbf{U}^{-1}\mathbf{R}^{\mathrm{T}} \quad , \tag{2.4}$$

where $\mathbf{L}_p$ is the plastic velocity gradient given by $\mathbf{L}_p = \dot{\mathbf{F}}_p\mathbf{F}_p^{-1}$. Assuming elastic strains are very small ($\mathbf{U} = \mathbf{I} + \boldsymbol{\epsilon}$ with $\|\boldsymbol{\epsilon}\| \ll 1$), Eq. 2.4 can be rewritten, neglecting $\boldsymbol{\epsilon}^2$ terms, as

$$\mathbf{L} = \dot{\mathbf{R}}\mathbf{R}^{\mathrm{T}} + \mathbf{R}\dot{\boldsymbol{\epsilon}}\mathbf{R}^{\mathrm{T}} - \mathbf{R}\dot{\boldsymbol{\epsilon}}\boldsymbol{\epsilon}\mathbf{R}^{\mathrm{T}} + \mathbf{R}\mathbf{L}_p\mathbf{R}^{\mathrm{T}} + \mathbf{R}\boldsymbol{\epsilon}\mathbf{L}_p\mathbf{R}^{\mathrm{T}} - \mathbf{R}\mathbf{L}_p\boldsymbol{\epsilon}\mathbf{R}^{\mathrm{T}} \quad . \tag{2.5}$$

From classic kinematics the velocity gradient is the sum of its skew and symmetric parts, $\mathbf{L} = \mathbf{D} + \mathbf{W} = \frac{1}{2}(\mathbf{L} + \mathbf{L}^{\mathrm{T}}) + \frac{1}{2}(\mathbf{L} - \mathbf{L}^{\mathrm{T}})$ [20]. Using Eq. 2.5, $\mathbf{D}$ and $\mathbf{W}$ can be written as

$$\mathbf{D} = \mathbf{R}\dot{\boldsymbol{\epsilon}}\mathbf{R}^{\mathrm{T}} + \mathbf{R}\mathbf{D}_p\mathbf{R}^{\mathrm{T}} + \mathbf{R}\boldsymbol{\epsilon}\mathbf{W}_p\mathbf{R}^{\mathrm{T}} - \mathbf{R}\mathbf{W}_p\boldsymbol{\epsilon}\mathbf{R}^{\mathrm{T}} \tag{2.6}$$

$$\mathbf{W} = \dot{\mathbf{R}}\mathbf{R}^{\mathrm{T}} + \mathbf{R}\mathbf{W}_p\mathbf{R}^{\mathrm{T}} + \mathbf{R}\boldsymbol{\epsilon}\mathbf{D}_p\mathbf{R}^{\mathrm{T}} - \mathbf{R}\mathbf{D}_p\boldsymbol{\epsilon}\mathbf{R}^{\mathrm{T}} - \frac{1}{2}(\mathbf{R}\dot{\boldsymbol{\epsilon}}\boldsymbol{\epsilon}\mathbf{R} - \mathbf{R}\boldsymbol{\epsilon}\dot{\boldsymbol{\epsilon}}\mathbf{R}) \tag{2.7}$$

with $\mathbf{D}_p$ and $\mathbf{W}_p$ being the symmetric and skew parts of $\mathbf{L}_p$ respectively. In Eq. 2.6 the terms containing $\dot{\boldsymbol{\epsilon}}\boldsymbol{\epsilon}$ and $\boldsymbol{\epsilon}\dot{\boldsymbol{\epsilon}}$ have been neglected because they are very small compared to $\dot{\boldsymbol{\epsilon}}$. To get the lattice rotation evolution relation, Eq. 2.7 can be solved for $\dot{\mathbf{R}}$,

$$\dot{\mathbf{R}} = \mathbf{W}\mathbf{R} + \mathbf{R}\left[-\mathbf{W}_p - \boldsymbol{\epsilon}\mathbf{D}_p + \mathbf{D}_p\boldsymbol{\epsilon} - \frac{1}{2}(\dot{\boldsymbol{\epsilon}}\boldsymbol{\epsilon} - \boldsymbol{\epsilon}\dot{\boldsymbol{\epsilon}})\right] \quad . \tag{2.8}$$

This equation can then be integrated to get the rotation tensor, $\mathbf{R}$.

2.2 Elasticity

Assuming that the Cauchy stress ($\boldsymbol{\sigma}$) is directly related to the elastic part of the deformation gradient through isotropic linear elasticity, the following relationship was adopted:

$$\boldsymbol{\sigma} = \mathbf{R}(\mathbf{C}\colon\boldsymbol{\epsilon})\mathbf{R}^{\mathrm{T}} \quad , \tag{2.9}$$

where $\mathbf{C}$ is the fourth order stiffness tensor given by

$$\mathbf{C} = 2G\mathbf{I}\mathbf{I} + \lambda\mathbf{I}\otimes\mathbf{I} \quad . \tag{2.10}$$

The assumption of isotropy was validated by McDonald [3], and was based on simulations and laboratory measurements. In Eq. 2.10, $\mathbf{I}\mathbf{I}$ is the fourth-order identity tensor and G and λ are the Lamé constants. Combining Eq. 2.9 and 2.10, the Cauchy stress in the current frame is given by

$$\boldsymbol{\sigma} = 2G\mathbf{R}\boldsymbol{\epsilon}\mathbf{R}^{\mathrm{T}} + \lambda\mathrm{tr}(\boldsymbol{\epsilon})\mathbf{I} \quad . \tag{2.11}$$

2.3 Plasticity

As discussed in this chapter's introduction, it was assumed that the plastic portion of the deformation is only due to lattice slip on slip planes. In other words $\mathbf{L}_p$ can be expressed as a function of the slip system shear rate ($\dot{\gamma}^s$) by the expression

$$\mathbf{L}_p = \sum_s \dot{\gamma}^s \mathbf{b}_o^s \otimes \mathbf{n}_o^s \quad , \tag{2.12}$$

where $\mathbf{b}_o^s$ and $\mathbf{n}_o^s$ are unit vectors in the reference configuration directed along the slip direction and the slip plane normal respectively for each slip system (s) [21].

It is now necessary to adopt a constitutive equation for the slip system shear rate ($\dot{\gamma}^s$) as a function of the resolved shear stress (τ^s) acting on the slip plane in the slip direction. The power law approximation used for this relation is often attributed to Hutchinson [17], who was seeking a constitutive relationship to describe crystal behavior under steady creep at constant temperature in the form

$$\dot{\gamma}^s = \dot{\gamma}_o \left| \frac{\tau^s}{\tau_0^s} \right|^n \operatorname{sign}(\tau^s) \quad , \tag{2.13}$$

where τ_0^s is the flow stress at a reference shear rate ($\dot{\gamma}_0$). However, this power law is not physically based, so the work of Follansbee & Kocks [18] was adopted for this investigation; Eq. 2.13 will serve as a numerical means for developing a unique partition of slip system shear rates. Their work predicts flow stress as a function of strain rate, temperature and a current state variable known as the mechanical threshold stress (MTS). The MTS ($\hat{\tau}$) is defined as the flow stress at 0 K.

The rate dependence of Eq. 2.13 is effectively removed by setting the value of n to a numerically convenient value (usually 20) and replacing the reference shear rate with the current macroscopic uniaxial equivalent plastic strain rate ($\dot{\boldsymbol{\varepsilon}}_p$), where

$$\dot{\boldsymbol{\varepsilon}}_p = \sqrt{\frac{2}{3}\left(\mathbf{D}_p : \mathbf{D}_p\right)} \quad . \tag{2.14}$$

The new constitutive equation is now given by

$$\dot{\gamma}^s = \dot{\boldsymbol{\varepsilon}}_p \left| \frac{\tau^s}{\tau_0^s} \right|^n \operatorname{sign}(\tau^s) \quad . \tag{2.15}$$

The MTS can be separated into two parts according to

$$\hat{\tau} = \hat{\tau}_a + \hat{\tau}_t \quad , \tag{2.16}$$

where $\hat{\tau}_a$ is the rate-independent athermal component associated with long range barriers to dislocations, and $\hat{\tau}_t$ is the rate-dependent thermal component, which characterizes the short range obstacles that can be overcome with thermal activation. The thermal component can further be broken down into two components $\hat{\tau}_i$ and $\hat{\tau}_\varepsilon$, which are respectively the thermal portion that does not evolve and the portion that describes the interaction with forest dislocations that does evolve. The MTS can now be expressed as

$$\hat{\tau} = \hat{\tau}_a + \hat{\tau}_i + \hat{\tau}_\varepsilon \quad . \tag{2.17}$$

The thermal components of the flow stress are related to their reference counterparts through the scaling functions $S_i\left(\dot{\boldsymbol{\varepsilon}}_p, T\right)$ and $S_\varepsilon\left(\dot{\boldsymbol{\varepsilon}}_p, T\right)$ so that $\tau_i = S_i\left(\dot{\boldsymbol{\varepsilon}}_p, T\right)\hat{\tau}_i$ and $\tau_\varepsilon = S_\varepsilon\left(\dot{\boldsymbol{\varepsilon}}_p, T\right)\hat{\tau}_\varepsilon$. The expressions for the scaling functions are given by

$$S_i = \left[1 - \left(\frac{kT}{g_{oi} G b^3} ln \frac{\dot{\varepsilon}_{oi}}{\dot{\boldsymbol{\varepsilon}}}\right)^{1/q_i}\right]^{1/p_i} \tag{2.18}$$

$$S_\varepsilon = \left[1 - \left(\frac{kT}{g_{o\varepsilon} G b^3} ln \frac{\dot{\varepsilon}_{o\varepsilon}}{\dot{\boldsymbol{\varepsilon}}}\right)^{1/q_\varepsilon}\right]^{1/p_\varepsilon} \quad , \tag{2.19}$$

where k is the Boltzmann constant, b is the magnitude of the burgers vector, g_o is the normalized activation energy for dislocations to overcome the obstacles, $\dot{\varepsilon}_o$ is a constant, T is the temperature, and *p* and *q* are statistical constants that characterize the geometry of the obstacles. Using this relationship, the flow stress of all the slip systems of a single crystal (τ_o) can be expressed in a similar fashion to the MTS itself as

$$\frac{\tau_o}{G} = \frac{\hat{\tau}_a}{G} + S_i\left(\dot{\boldsymbol{\varepsilon}}_p, T\right)\frac{\hat{\tau}_i}{G_o} + S_\varepsilon\left(\dot{\boldsymbol{\varepsilon}}_p, T\right)\frac{\hat{\tau}_\varepsilon}{G_o} \tag{2.20}$$

where G_o is a reference value of the shear modulus G, which is modeled by [22]

$$G = G_o - \frac{D_o}{exp\left(\frac{T_o}{T}\right) - 1} \tag{2.21}$$

where D_o and T_o are empirical constants.

The evolution of $\hat{\tau}_\varepsilon$, which can be thought of as the hardening component of the MTS model, is associated with the mechanism of forest hardening. The reader is reminded that a detailed discussion of this evolution, including the implementation of stage IV hardening, can be found in Kok's dissertation [19].

3 Cohesive Failure and the Traction-Separation Laws

The basic ideas behind the cohesive failure model can be found in the avant-garde work of Dugdale and Barrenblatt in the early 1960s [23, 24], which introduced the concept of a plastic zone ahead of a crack tip and characterized the stresses present inside of its boundary. Their work served as a basis to provide some structure to the failure process taking place in the vicinity of a crack tip. To allow for material softening, spontaneous initiation of fracture surfaces, and the propagation of those surfaces, a series of cohesive zone elements of zero thickness can be introduced within a finite element mesh. These cohesive elements act like nonlinear springs linking adjacent surfaces of volumetric finite elements at interfaces where failure is possible. These nonlinear springs resist opening by imposing cohesive tractions $(\mathcal{T})$ in accordance with a prescribed traction-separation relation. These tractions, functions of the crack opening displacement (δ), typically vanish for a critical value (δ_c) . When δ_c is reached, the interface starts losing cohesion and gradually softens until a stress-free surface is created [25]. Figure 3.1 is a schematic of a cohesive zone model for an edge crack illustrating the previous discussion in the 2-D case. This method is popular because cohesive elements eliminate the singularities ahead of the crack tip that are often associated with linear elastic fracture mechanics (LEFM).

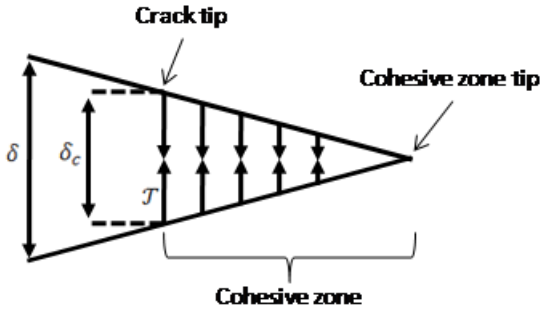

Figure 3.1: Schematic representation of cohesive traction acting on an edge crack subjected to tensile loading.

3.1 Traction-Separation Laws

The essence of the cohesive zone approach is the relationship between the tractions acting on the interface and the corresponding displacement discontinuities (or crack opening displacements). The two original cohesive failure models available in the literature are the *extrinsic* linear law developed by Camacho and Ortiz [26], and the *intrinsic* exponential potential-based law developed by Xu and Needleman [27]. The distinction between the two approaches is associated with the way the damage initiation process is modeled.

3.1.1 Extrinsic Linear Traction-Separation Law

In the *extrinsic* case, the external stress-based failure criterion is based on LEFM, and is given by

$$\sigma_f = \frac{K_{Ic}}{\sqrt{\pi a_0}} \quad , \tag{3.1}$$

where a_0 is the half width of an internal crack and K_{Ic} is the material fracture toughness. This failure criterion is external to the cohesive elements in the sense that it is based on the bulk behavior of the material. The fracture stress (σ_f) is compared to an effective traction ($\boldsymbol{\mathcal{T}}_e$) given by:

$$\boldsymbol{\mathcal{T}}_e = \begin{cases} \sqrt{\mathcal{T}_n^2 + \beta \mathcal{T}_s^2} & \text{for } \mathcal{T}_n \geq 0 \\ \sqrt{\beta}(|\mathcal{T}_s| - \mu|\mathcal{T}_n|) & \text{for } \mathcal{T}_n < 0 \end{cases} \quad , \tag{3.2}$$

where μ is the friction coefficient, β is a shear stress factor assigning different weights to the shear stresses, and the subscripts n and s stand for the normal and shear components respectively. This effective stress characterizes the amplitude of the tractions acting on the interface. When the effective traction is equal to or greater than the fracture stress, a cohesive interface is introduced by replacing every node at this threshold stress with two nodes. The relative displacements of these two nodes (δ) follow a traction-separation relation of the form

$$\mathcal{T}_n = \mathcal{T}_{nc}\left(1 - \frac{\delta_n}{\delta_{nc}}\right) \tag{3.3}$$

$$\mathcal{T}_s = \mathcal{T}_{sc}\left(\frac{\delta_n}{\delta_{nc}}\right)\text{sign}(\delta_s) \quad , \tag{3.4}$$

where $\mathcal{T}_{nc}$and $\mathcal{T}_{sc}$ are the normal and shear tractions at initiation of fracture and δ_{nc} is the normal displacement jump at complete separation.

The cohesive law in the absence of compression takes the linear form seen in figures 3.2a-b. Damage is made irreversible by remembering the maximum displacement jump achieved in the simulation and using it for the unloading and subsequent reloading path. For example, consider the normal traction cohesive law in figure 3.2a. If the model was loaded to point A and then subsequently unloaded, it would follow a path straight back to the origin as shown. Upon further loading, the behavior would follow its unloading path back to A and then continue onward to point B.

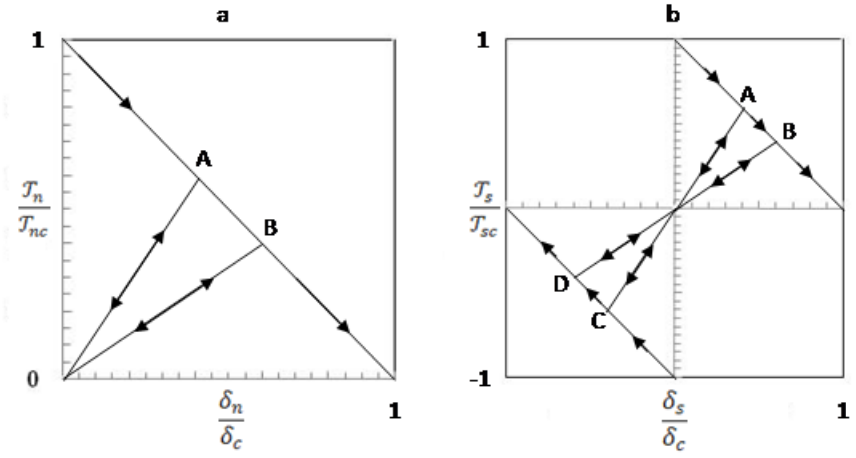

Figure 3.2: Camacho and Ortiz' (a) normal and (b) shear cohesive traction-separation law [adapted from 28].

Among the advantages of this method is the fact that it accounts for permanent damage and, because it is developed in the absence of the traction-separation law, the stress field prior to failure is unaffected by the cohesive elements. Furthermore, since cohesive elements are only introduced upon the detection of local failure, the initiation of a crack can occur anywhere in the model and the path of its growth is not constrained

to any specific direction. This method, however, doesn't couple the normal and tangential relations between the displacement jumps and tractions and thus requires intensive bookkeeping to account for the dynamic addition of nodes and the associated renumbering process [28].

3.1.2 Potential-Based Intrinsic Traction-Separation Law

The model developed by Xu and Needleman uses a potential-based *intrinsic* cohesive approach, in which the cohesive tractions are derived from a scalar decohesion potential ϕ as

$$\boldsymbol{\mathcal{T}} = -\frac{\partial \phi}{\partial \boldsymbol{\Delta}} \quad . \tag{3.5}$$

Here $\boldsymbol{\mathcal{T}}$ is the traction vector and $\boldsymbol{\Delta}$ is the displacement jump vector. The form of the decohesion potential used in their 2-D analyses is

$$\begin{aligned} \phi(\boldsymbol{\Delta}) = \phi_n + \phi_n \exp\left(-\tilde{\delta}_n\right)\Bigg\{\left[1 - r + \tilde{\delta}_n\right]\left(\frac{1-q}{r-1}\right) \\ - \left[q + \left(\frac{r-q}{r-1}\right)\tilde{\delta}_n\right]\exp\left(-\tilde{\delta}_s^2\right)\Bigg\} \end{aligned} \tag{3.6}$$

where $\phi_n = \exp(1)\mathcal{T}_{nc}\delta_{nc}$ and $\phi_s = \sqrt{\frac{\exp(1)}{2}}\mathcal{T}_{sc}\delta_{sc}$ are the energies of separation for the normal and shear case respectively, r is the value of the normal displacement jump after complete shear failure ($\mathcal{T}_n = 0$), $q = \frac{\phi_s}{\phi_n}$, and $\tilde{\delta}_n$ and $\tilde{\delta}_s$ are defined in Eq. 3.7 below:

$$\begin{Bmatrix} \tilde{\delta}_n \\ \tilde{\delta}_s \end{Bmatrix} = \begin{Bmatrix} \frac{\delta_n}{\delta_{nc}} \\ \frac{\delta_s}{\delta_{sc}} \end{Bmatrix} \quad . \tag{3.7}$$

The resulting normal and shear traction components (after the simplifying assumptions $q = 1$ and $r = 0$) reduces to [28]

$$\mathcal{T}_n = \begin{cases} -\mathcal{T}_{nc}\tilde{\delta}_n \mathrm{e}^{1-\tilde{\delta}_n-\tilde{\delta}_s^2} & \delta_n > 0 \\ -\mathcal{T}_{nc}\tilde{\delta}_n \mathrm{e} & \delta_n < 0 \end{cases}, \qquad \mathcal{T}_s = -2\mathcal{T}_{nc}\frac{\delta_{nc}}{\delta_{sc}}\tilde{\delta}_s\left(1+\tilde{\delta}_n\right)e^{1-\tilde{\delta}_n+\tilde{\delta}_s^2} \tag{3.8}$$

and is shown in figures 3.3a-b.

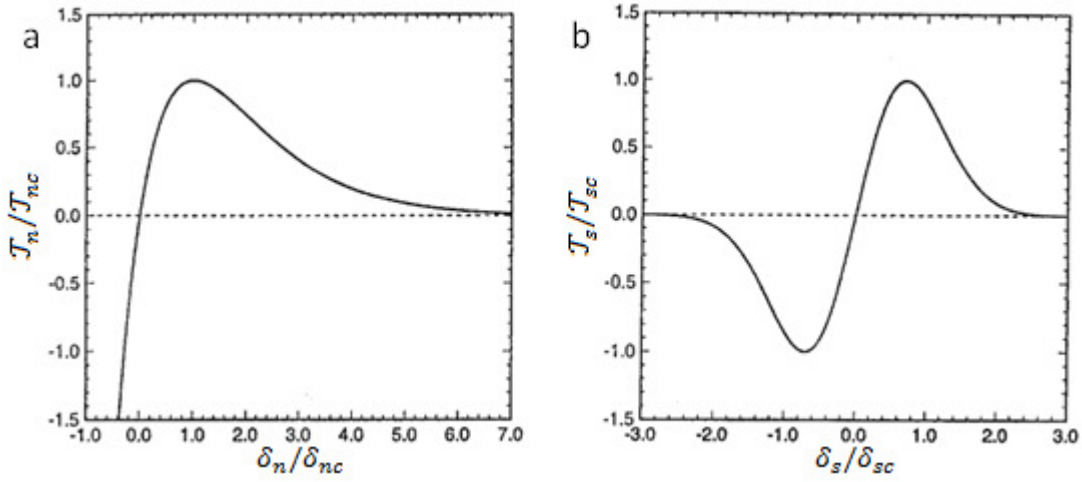

Figure 3.3: The intrinsic potential-based exponential cohesive model in (a) pure tension and (b) pure shear [adapted 27].

The greatest advantage of the *intrinsic* approach lies in its simplicity of numerical implementation. Because all of the cohesive elements are present at the onset of the finite element analysis and the mesh remains unchanged, there is no need for adaptive meshing as in the *extrinsic* approach [28]. However the presence of cohesive elements with initial elasticity brings forward the argument of Klein *et al.* [29] that initial elasticity artificially lowers the stiffness of the material. To prevent this, the initial slope of the traction-separation law should be as steep as possible so rigidity can be approximated. This loss of stiffness makes the *intrinsic* approach best suited for cases where the interfaces are intended to model the position of a known physical interface such as grain boundaries [30], which is the case for the model in the present work.

From the discussion above, it is evident that the *intrinsic* and *extrinsic* methods have their advantages and disadvantages depending on their application, but they are both attempting to describe the same physical phenomenon. While dissimilar in appearance, the shapes of their traction-separation curves do not have a big effect on

the resulting fracture process. However, the values of the maximum attainable traction and critical crack opening displacement do play an important role [31]. In general the energy required to create a new fracture surface, the critical energy release rate G_c, corresponds to the area below the traction-separation curve and is defined by

$$G_{Ic} = \int_0^{\infty} \mathcal{T}_n \, d\delta_n \tag{3.9}$$

$$G_{IIc} = \int_0^{\infty} \mathcal{T}_s \, d\delta_s \quad , \tag{3.10}$$

where $\mathcal{T}$ and δ are the traction and crack opening displacement respectively [32].

3.2 Bilinear Cohesive Law

The cohesive formulation used in this work is based on the initially elastic model developed by Ortiz and Pandolfi [32] in its bilinear form. This law, presented for comparison to an initially rigid bilinear cohesive law in papers by Papoulia and her coworkers [33], is given by

$$\delta_e = \sqrt{\beta_\tau^2 \delta_s^2 + \langle \delta_n \rangle^2} \tag{3.11}$$

$$\mathcal{T}_e = \begin{cases} \mathcal{T}_c \delta_e / \delta_{soft} & \text{if } \delta_e < \delta_{soft} \\ \mathcal{T}_c (\delta_c - \delta_e) / (\delta_c - \delta_{soft}) & \text{if } \delta_{soft} \le \delta_e < \delta_c \\ 0 & \text{elsewhere} \end{cases} \tag{3.12}$$

$$\boldsymbol{\mathcal{T}} \equiv (\mathcal{T}_s, \mathcal{T}_n) = \begin{cases} \mathcal{T}_e (\beta_\tau^2 \delta_s / \delta_e, \delta_n / \delta_e) \, , & \text{if } \delta_n \ge 0 \\ (\beta_\tau^2 \mathcal{T}_e \delta_s / \delta_e, k_c \delta_n) \, , & \text{if } \delta_n < 0 \end{cases} \quad . \tag{3.13}$$

The subscript e denotes a non-negative effective scalar value and the subscripts n and s represents the normal and shear components respectively. The parameter β_τ is the shear stress factor (not to be confused with β from Eq. 3.2) and the MacCaulay bracket operator ("⟨ ⟩") is defined as

$$\langle x \rangle = \begin{cases} x & \text{if } x \ge 0 \\ o & \text{else} \end{cases} \quad . \tag{3.14}$$

Notice in Eq. 3.1-3.13, there is no distinction between the critical values of the normal and shear components. This is because the law uses effective values of traction and crack opening displacement which couples their normal and shear components,

therefore only one critical value for the cohesive zone needs to be defined. The effective critical opening displacement (δ_c) is the point when complete failure occurs and δ_{soft} is the displacement at which the material stops hardening and begins to soften. Interpenetration of cohesive surfaces is counteracted by imposing resisting forces through a penalty parameter k_c. This initially elastic model is illustrated in figure 3.4 below.

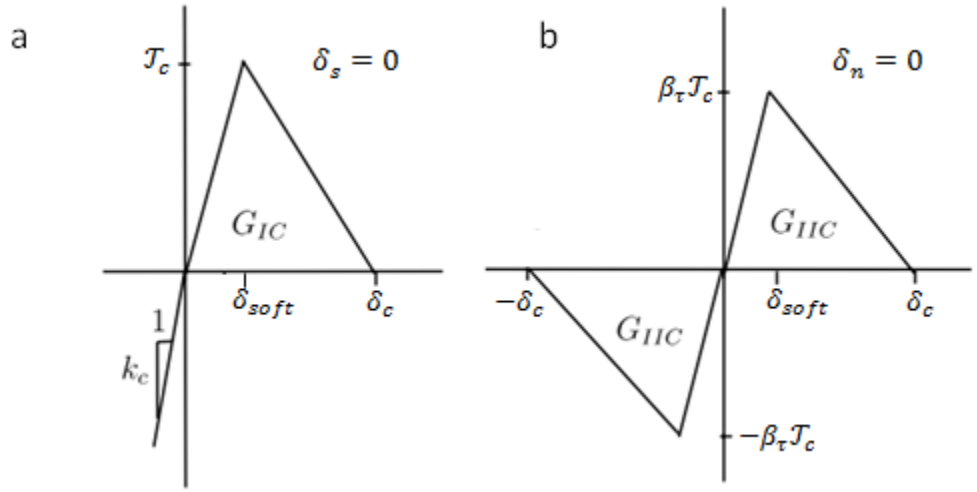

Figure 3.4: Bilinear initially elastic traction-separation law for (a) pure Mode I and (b) pure mode II deformation [adapted 33].

This model draws from both the *intrinsic* and *extrinsic* methods discussed previously. It uses a potential based constitutive model like Xu and Needleman's *intrinsic* model (albeit in a different form), and it couples the normal and tangential components of the traction and opening vectors through the use of effective displacement (δ_e)and traction ($\mathcal{T}_e$) values. Irreversibility of damage, an advantage of the *extrinsic* model of Camacho and Ortiz, is implemented through encoding a strength parameter $\lambda_{max}(t')$ such that

$$\lambda_{max}(t') = \frac{\max\limits_{t\in[t_0,t']} \delta_e(t)}{\delta_c} \quad , \tag{3.15}$$

where a point is considered unloading at time t' when $\lambda(t') < \lambda_{max}(t')$, where $\lambda(t') = \frac{\delta_e(t')}{\delta_c}$. The cohesive traction can then be calculated, by assuming a linear unloading/reloading path that passes through the origin.

4 Finite Element Model

This work considers a one tenth portion at the center of a compact tension (C(T)) specimen, which is shown in figure 4.1a. At the onset of stable crack growth, the plastic zone size in the vicinity of the crack tip is small with respect to the dimensions of the C(T) specimen. It is therefore possible to use a small scale yielding (SSY) modeling approach.

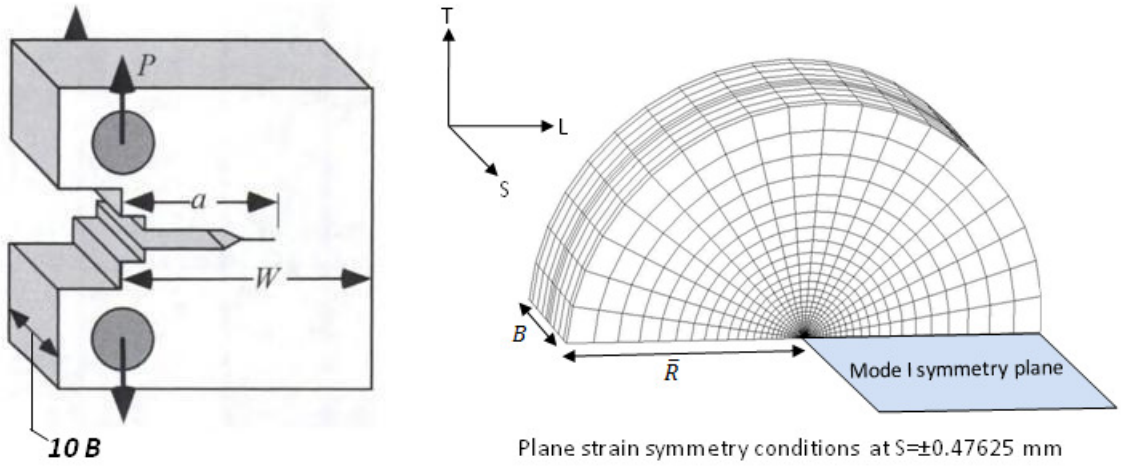

Figure 4.1: (a) Schematic of C(T) specimen [adapted 11]. (b) Finite element mesh for 3D small-scale-yielding analyses scaled for clarity.

The SSY model consists of an edge crack and a large region of material enclosing the crack front (figure 4.2b). The specific model constructed for this work has thickness B=0.95 mm. The boundary of the domain lies at a radius $\bar{R}$ = 1000B, such that the plastic zone for the primary crack front remains well confined within the linear elastic region at maximum load and does not interact with the boundary. The model uses eight-node brick elements whose constitutive behavior follows the elasto-viscoplastic MTS model described in chapter 2. It contains 10 layers of elements through the thickness. The layer thicknesses starting at the mid-plane and moving outward (S > 0) are 0.053B, 0.104B, 0.133B, 0.133B, 0.076B. This progression of layer thickness also holds for the opposite side of the model (S < 0). The symmetry of the Mode I configuration allows modeling of only one half of the domain and implies that the growth of the delamination is

symmetric both above and below the primary crack plane, which may not always be the observed behavior.

Simulation of the primary and delamination crack's fracture processes were done by inserting cohesive zone elements, as outlined in chapter 3, into the SSY model on two planes. The first cohesive zone, simulating the primary crack, was placed in the $\mathrm{T} = 0$ mm plane extending from $\mathrm{L} = 0$ mm to $\mathrm{L} = 1.88$ mm across the entire thickness. The second cohesive zone, simulating the delamination crack was placed in the $\mathrm{S} = 0$ mm plane extending from (L,T) = (-1.93,0) mm to (L,T) = (1.93,1.02) mm.

Loading of the model occurs through displacements imposed on the remote cylindrical boundary at $\bar{R}$ by in-plane components ($u_{\mathrm{L}}, u_{\mathrm{T}}$) that follow the linear elastic, plane-strain (Mode I) field for a specified K_I value [11],

$$u_{\mathrm{L}} = \frac{K_I}{2G}\sqrt{\frac{\bar{R}}{2\pi}}\cos\left(\frac{\theta}{2}\right)\left[\kappa - 1 + 2\sin^2\left(\frac{\theta}{2}\right)\right] \tag{4.1}$$

$$u_{\mathrm{T}} = \frac{K_I}{2G}\sqrt{\frac{\bar{R}}{2\pi}}\sin\left(\frac{\theta}{2}\right)\left[\kappa + 1 - 2\cos^2\left(\frac{\theta}{2}\right)\right] \tag{4.2}$$

$$u_{\mathrm{S}} = 0 \tag{4.3}$$

where u_{L} is the displacement parallel to the crack (in the L direction), u_{T} is the displacement normal to the crack plane (in the T direction), $\kappa = (3 - 4\nu)$, ν is Poisson's ratio, G is the shear modulus, $\bar{R}$ is the radius of the SSY model domain, and K_I is the specified stress-intensity factor. These displacements remain uniform at each node through the thickness on the outer boundary of the model. Loading progresses by imposing a K_I value at a specific time through displacements computed from Eq. 4.1-4.3.

5. Results and Discussion

Whether or not the material is going to delaminate depends on several factors such as toughness, texture, and the magnitude of the driving forces. The toughness depends on material properties and microstructure, which can vary greatly depending on the how the material is processed. On the other hand, the driving force is a consequence of the geometry and loading, which may include grain orientation (texture) and the location of the primary crack. The effects of these factors on the behavior of the delamination process are the motivation for this study. This chapter begins with a brief presentation of the model parameters and an overview of the simulated results. The overview aims at familiarizing the reader with how the simulation progresses and how the results are presented. Second, a validation of the models predictive capabilities is presented. Finally, results of the parametric studies performed are discussed.

5.1 Model parameters

The simulation parameters used in this study (unless otherwise noted) can be separated in to three categories: material properties, cohesive-zone parameters, and crystallographic orientations. The material properties include elastic and plastic parameters such as the bulk modulus (K) and the athermal portion of the flow stress (τ_a). These parameters are discussed in detail in chapters 2.2 and 2.3 and are listed in table 5.1. Cohesive-zone parameters are listed in Table 5.2 and include the critical traction and displacement as discussed in chapter 3.2. It should be noted that all of these parameters were chosen to represent a typical Al-Li alloy at room temperature. The crystallographic orientations considered in this study are presented in Kocks notation (table 5.3) as well as [100], [110], and [111] pole figures (figure 5.1). A pole figures is a projection of a set of crystallographic directions relative to the laboratory reference frame. For example, the [100] pole figure is the projection of all face normals of the crystallographic unit cell such that the cube orientation has poles at the center and on the periphery of the projection [34]. As a reminder to the reader the orientations

used were not chosen at random but motivated by EBSD studies which are described in the introduction (figures 1.4 and 1.5).

Table 5.1 Material Properties

Parameter	Value	Pertinent Equations
G_0	34620 MPa	2.21, 2.20
τ_a	7.3956 MPa	2.20
τ_i	380.82 MPa	2.20
g_{0i}	2.3376	2.18
$g_{0\varepsilon}$	1.6	2.19
p_i	1/2	2.18
p_ε	2/3	2.19
q_i	3/2	2.18
q_ε	1	2.19
ε_{0i}	$1x10^{13}$	2.18
$\varepsilon_{0\varepsilon}$	$1x10^{7}$	2.19
D_0	3000	2.21
T_0	180	2.21
ν	0.3	4.1, 4.2
$\frac{k}{b^3}$	0.823 MPa/K	2.18, 2.19
K	60973.81 MPa	*2.11

*The bulk modulus K is used in conjunction with G from equation 2.21 to compute the second Lamé constant λ.

Table 5.2 Cohesive Zone Parameters

	Primary Crack	Delamination
$\mathcal{T}_c$	1350 MPa	675 MPa
δ_c	0.0167 mm	0.00667 mm
δ_{soft}	0.000833 mm	0.000333 mm
β_τ	2	0.5
k_c	5	5

Table 5.3 Crystallographic Orientations in Kocks Notation

Name	ψ	Θ	ϕ
Cube	0˚	0˚	0˚
S	31˚	43˚	-153˚
Brass_1	55˚	45˚	0˚
Brass_2	35˚	90˚	45˚

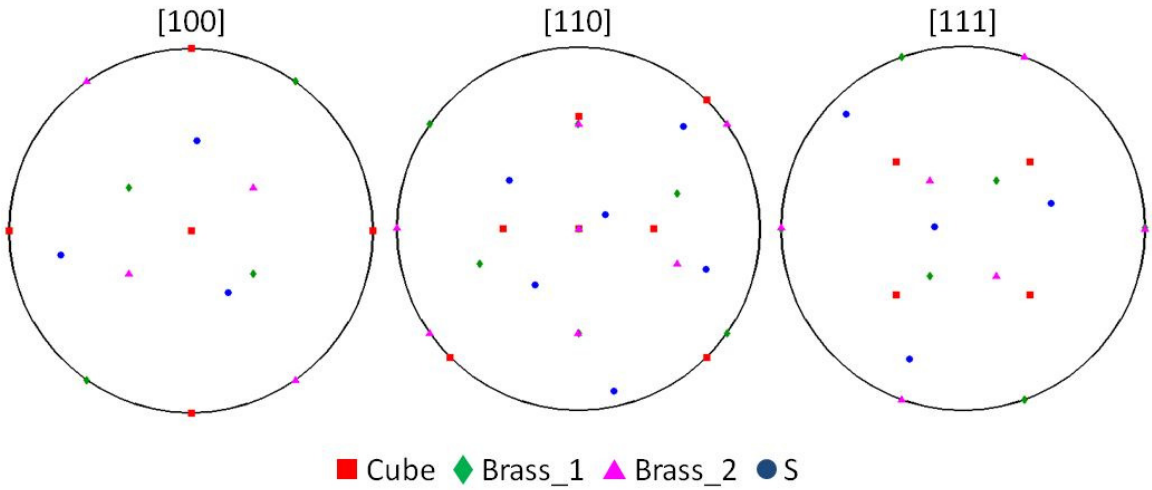

Figure 5.1: Pole figures showing the chosen orientations of the simulations.

5.2 Overview of Typical Results

The purpose of this section is to familiarize the reader with the results of the simulations. These results include the evolution of the primary and delamination crack-fronts and their corresponding stress fields. More specifically a homogeneous bi-crystal using the cube orientation and the typical material properties is considered here.

5.2.1 Crack Front Growth

The behavior of dynamic crack growth on both the primary crack and delamination planes are shown at five different load steps (11.82, 14.14, 18.47, 23.38, and 28.87 kJ/m^2) in figures 5.2a-b. The first noticeable feature in the plots is that the delamination begins to grow at lower loads as compared to the primary crack. (This is evidenced by the absence of any primary crack extension at the first two load steps in figure 5.2a.) This suggests that even though the applied load is Mode I for the primary crack, the complex state of stress developed ahead of the primary crack quickly creates stresses at levels that easily nucleate delaminations. This makes sense because the grain boundary interface strength (in shear) is about half that of the material strength [35]. The second, and debatably the most interesting trend, shown in the plots is the "V"-shaped primary crack front. This suggests that the stresses that drive the primary crack growth are severely impacted by the presence of the delamination. This trend will be discussed in more detail subsequently. It is also noticed that the rate of crack extension for both the primary crack and delamination starts high and then decreases as the applied load is progressed.

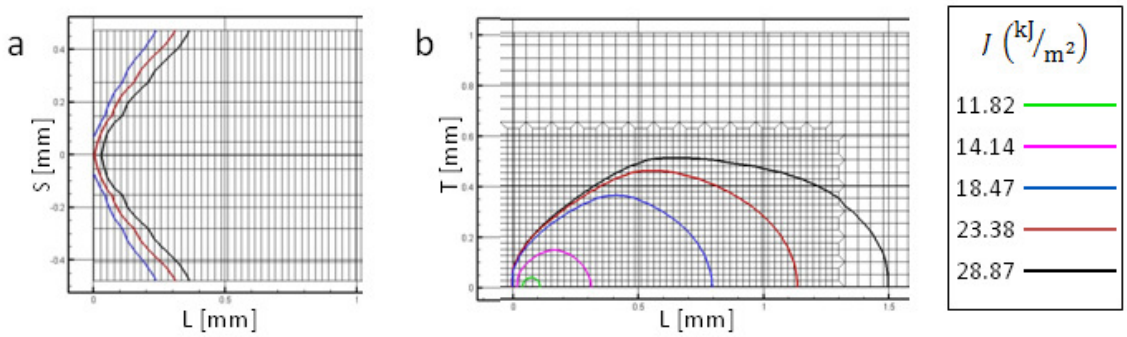

Figure 5.2: (a) Primary crack front and (b) delamination front at various applied loads.

5.2.2 Stress Field on the Center Plane Ahead of the Primary Crack

Figures 5.3a-c show the stress contours of σ_{LL}, σ_{TT}, and σ_{SS} (normalized by the yield stress σ_0) on the LS-plane (primary crack plane) at an applied load of $J = 16.67$ kJ/m^2. All of these figures have three main features in common at $\mathrm{S} = 0$: (1) a peak stress very close to the primary crack front indicating some loss of through thickness constraint, (2) a zone with low stress values in the area of the delamination crack, and (3) a secondary peak developing just ahead of the leading edge of the delamination crack front. As an example, refer to the opening mode stress σ_{TT} (figure 5.3b), where a peak stress is developed at $\mathrm{L} = 0.05$ mm of $\sigma_{\mathrm{TT}} = 1.35\sigma_0$ that immediately reduces to $\sigma_{\mathrm{TT}} \approx 0.75\sigma_0$ in the area of the delamination. The loss of through thickness constraint is evident in the area of the delamination crack, because stress values maintain this $0.75\sigma_0$ value over its entirety. Progressing past the leading edge of the delamination ($L \approx 0.6$ mm), a secondary peak of $\sigma_{\mathrm{TT}} = 1.95\sigma_0$ develops as the through thickness constraint is restored.

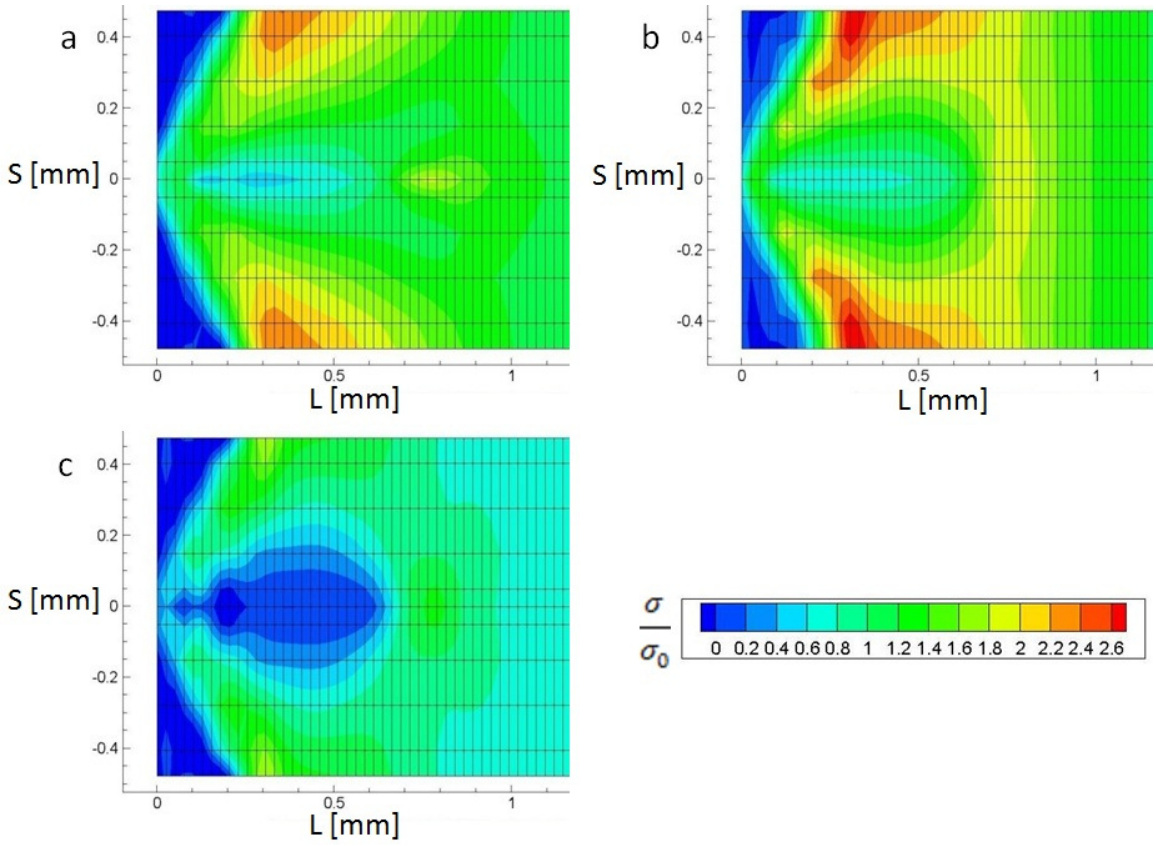

Figure 5.3: (a) σ_{LL}, (b) σ_{TT}, and (c) σ_{SS} stress contour plots on the primary crack plane at applied an applied load $J = 16.67$ kJ/m^2. All stress components have been normalized by yield stress σ_0.

The data presented in figures 5.3a-c indicates that the delamination effectively splits the primary crack and relieves the through thickness stress creating a plane stress condition at the newly formed free surfaces. This significantly reduces the primary crack driving force on the center plane effectively slowing down the growth of the primary crack. This trend is evident when plotted on a J vs Δa curve (figure 5.4). As the load progresses through the simulation, the rate of crack growth decreases. This effect points to the position that crack divider delaminations can actually be beneficial in terms of failure.

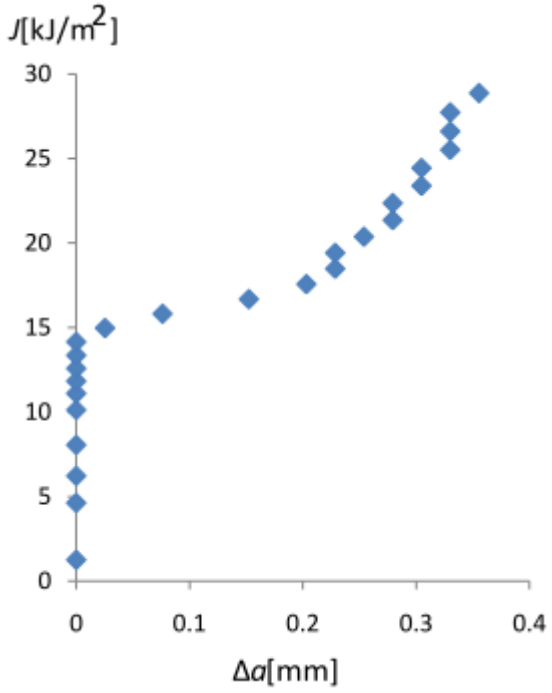

Figure 5.4: Plot of applied load versus maximum primary crack extension.

5.2.3 Primary Crack Driving Forces

This section describes the stresses that drive the growth of the primary crack. Figures 5.5a-b show two types of plots of the effective stress on the primary crack plane at an applied load of $J = 16.67$ kJ/m^2. As an aside, this effective stress can be thought of as an interpretation of strength on an interface and is given by [32]

$$\sigma_e = \sqrt{\sigma_{\mathrm{TT}}^2 + \frac{1}{\beta_\tau}(\sigma_{\mathrm{LT}}^2 + \sigma_{\mathrm{TS}}^2)} \tag{5.1}$$

$$\sigma_e = \sqrt{\sigma_{\mathrm{SS}}^2 + \frac{1}{\beta_\tau}(\sigma_{\mathrm{LS}}^2 + \sigma_{\mathrm{TS}}^2)} \tag{5.2}$$

for the primary crack plane and delamination plane respectively. Figure 5.5a is a straight forward contour plot where as Figure 5.5b is a plot of this effective stress at both the center plane ($\mathrm{S} = 0$ mm) and the edge ($\mathrm{S} = 0.47625$ mm). In both plots the effective stress has been normalized by the cohesive strength of the primary crack $\mathcal{T}_c = 1350$ MPa. It was found that the shear stress components are negligible fractions of the yield

stress and therefore the effective stress is dominated by the mode I opening stress σ_{TT}. From figure 5.5, it is easily seen that the leading edge of the primary crack reaches effective stress values on the order of the primary crack cohesive strength indicating crack growth. On the other hand, the stress at the center plane shows the same attenuated behavior discussed in the previous section, which further illustrates the suppressive nature of the delamination on the primary crack driving forces.

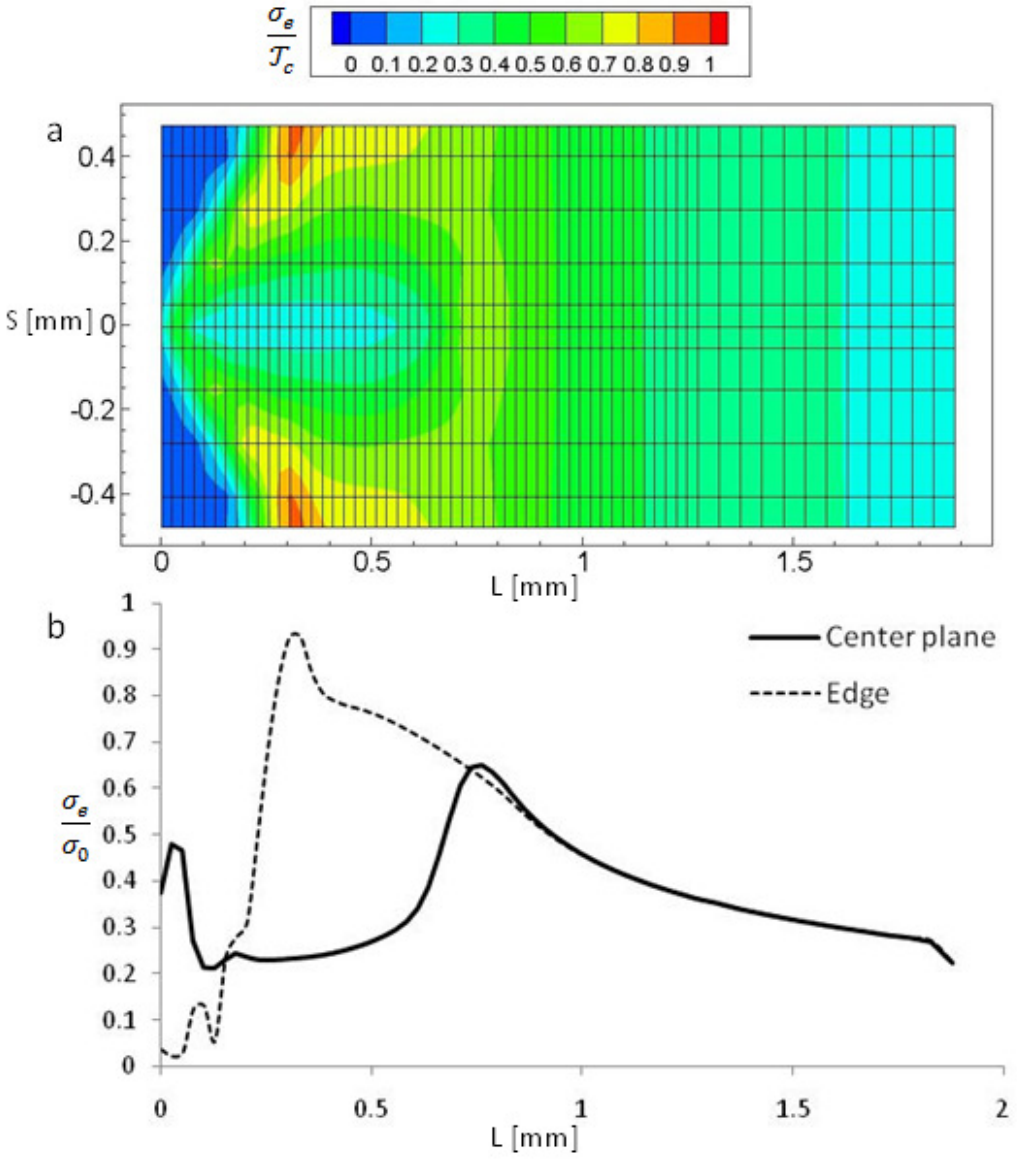

Figure 5.5: (a) A plot showing the contours of the effective stress resolved on the cohesive zone element (σ_e). (b) A plot of σ_e at both the center plane and edge of the primary crack plane. Both plots normalize σ_e by the cohesive strength and are at an applied load of $J = 16.67$ kJ/m^2.

5.2.4 Delamination Crack Driving Forces

In previous sections it was shown that the driving forces at the center plane near the primary crack front are diminished by the presence of a delamination crack, slowing its advance. In this section the diving stresses of the delamination crack are studied. Figures 5.6a-c show the σ_{SS}, σ_{TS}, and σ_{LS} stress components (normalized by the yield stress) on the LT-plane at $\mathrm{S} = 0$mm under a loading of $J = 16.67$ kJ/m^2. The reader is reminded that σ_{SS} is the opening mode stress for the delamination.

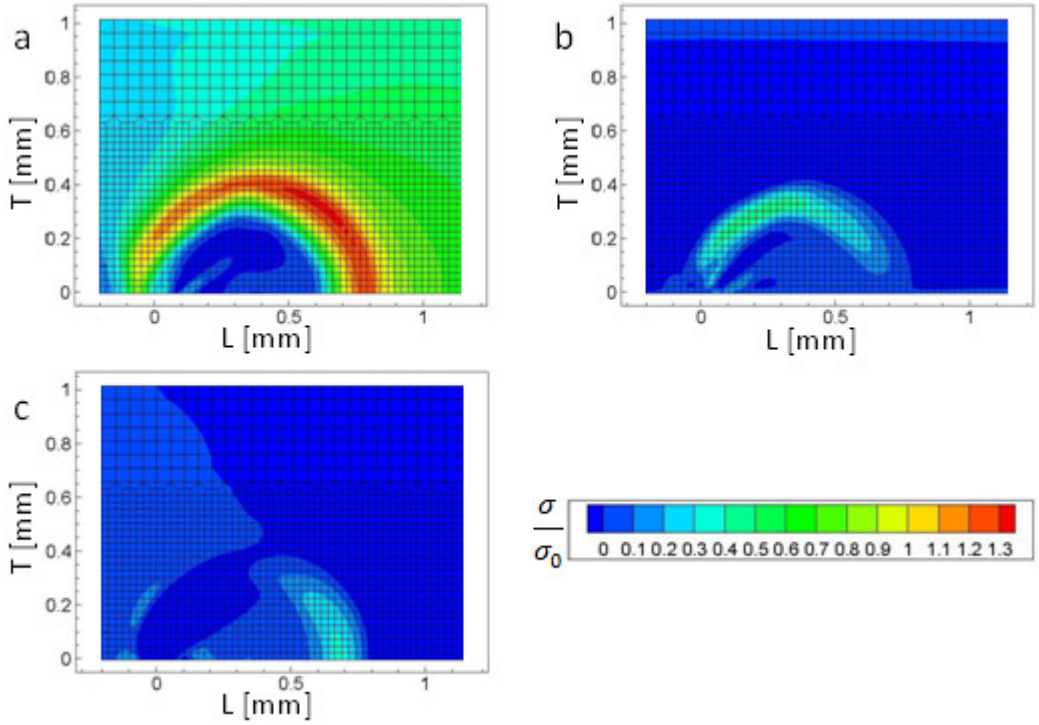

Figure 5.6: Contour plots of (a) σ_{SS}, (b) σ_{TS}, and (c) σ_{LS} at an applied load of $J = 16.67$ kJ/m^2. All stress components have been normalized by the cohesive strength.

All of the stresses shown in figure 5.6 reach peak values around the leading edge of the delamination, which extends in the L direction to approximately 0.6 mm. Unlike the primary crack driving stresses, the shear components of stress are not negligible. Not only are these shears significant, since the strength of the delamination interface has been shown to be very weak in shear, these stresses are potentially more damaging than the opening mode stress [35]. The peak value of the opening mode stress

(corresponding to a significantly high state of hydrostatic tension) achieves a value of $1.32\sigma_0$, and the shears σ_{TS} and σ_{LS} reach values of $0.50\sigma_0$ and $0.34\sigma_0$ respectively.

The non-negligible shears make it important to look at the effective stress, which takes into account all three components. Shown in figure 5.7, the entire perimeter of the delamination is preceded by effective stresses in excess of $\sim 0.9\mathcal{T}_c$ ($\mathcal{T}_c = 675$ MPa). This data demonstrates that a self-generated localized stress field exists due to the delamination having a combination of shear and normal stress. This field has the potential to promote further extension of existing crack divider delaminations.

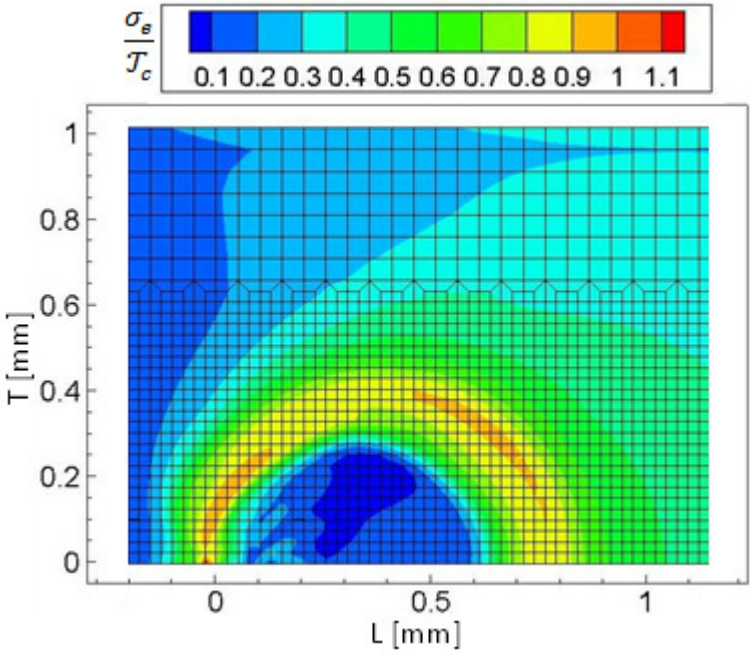

Figure 5.7: A contour plot of the effective stress normalized by cohesive strength on the delamination plane ($\mathcal{T}_c = 675$ MPa) at an applied load of $J = 16.67$ kJ/m^2.

5.3 Model Validation

This section presents data to validate the behavior of the model. To accomplish this task, the results of a simulation using the cube orientation for both sides of the bi-crystal was compared to data and simulation results collected by Kalyanam et al. [36]. Additionally a parametric study of fracture toughness was carried out to confirm the expected behavior.

Kalyanam and his colleagues performed similar studies of crack divider delaminations in 2099-T87 Al-Li alloy plate in order to characterize the stress states that serve to drive growth of the macro and delamination cracks. He used a 3-D small-scale yielding framework similar to the one used in the current study, but described the constitutive behavior by an isotropic hardening model utilizing a yield surface based on the bulk anisotropic response. To characterize this yield surface he used a combination of mechanical tests, texture analysis and metallographic observations, and applied it homogeneously to the entire finite element model. This was the basis for choosing a uniform orientation across the bi-crystal model, which effectively mirrors the homogeneity of Kalyanam's model. Using the cube orientation was intended to simulate near isotropic material behavior, which will serve as a base line simulation. It should be emphasized here that while the current study simulates the dynamic growth of both the macro and delamination cracks, Kalyanam's study introduced the delamination crack into the finite element model prior to any loading. The presence of a delamination crack perpendicular to the primary crack leads to significant disturbances in the stress state and fracture behavior of the material.

To compare the data of both studies, the stresses σ_{LL}, σ_{TT}, and σ_{SS} at an applied load of $J = 16.67$ kJ/m^2 are plotted over Kalyanam's data for the same stresses at an applied load of $J = 11.6$ kJ/m^2. The load values were chosen such that the delaminations were the same size, roughly 0.6 mm in the L direction. Although cube was chosen for the validation, a better agreement with Kalyanam's data may be expected from choosing an orientation that matched his measured bulk anisotropy. Furthermore, Kalyanam's work imposes monotonically increasing remote loads with no growth of the primary crack and no growth of the delamination crack. Consequently, unlike the current investigation, his results reflect no history effects of stable crack growth on the computed primary crack stress fields.

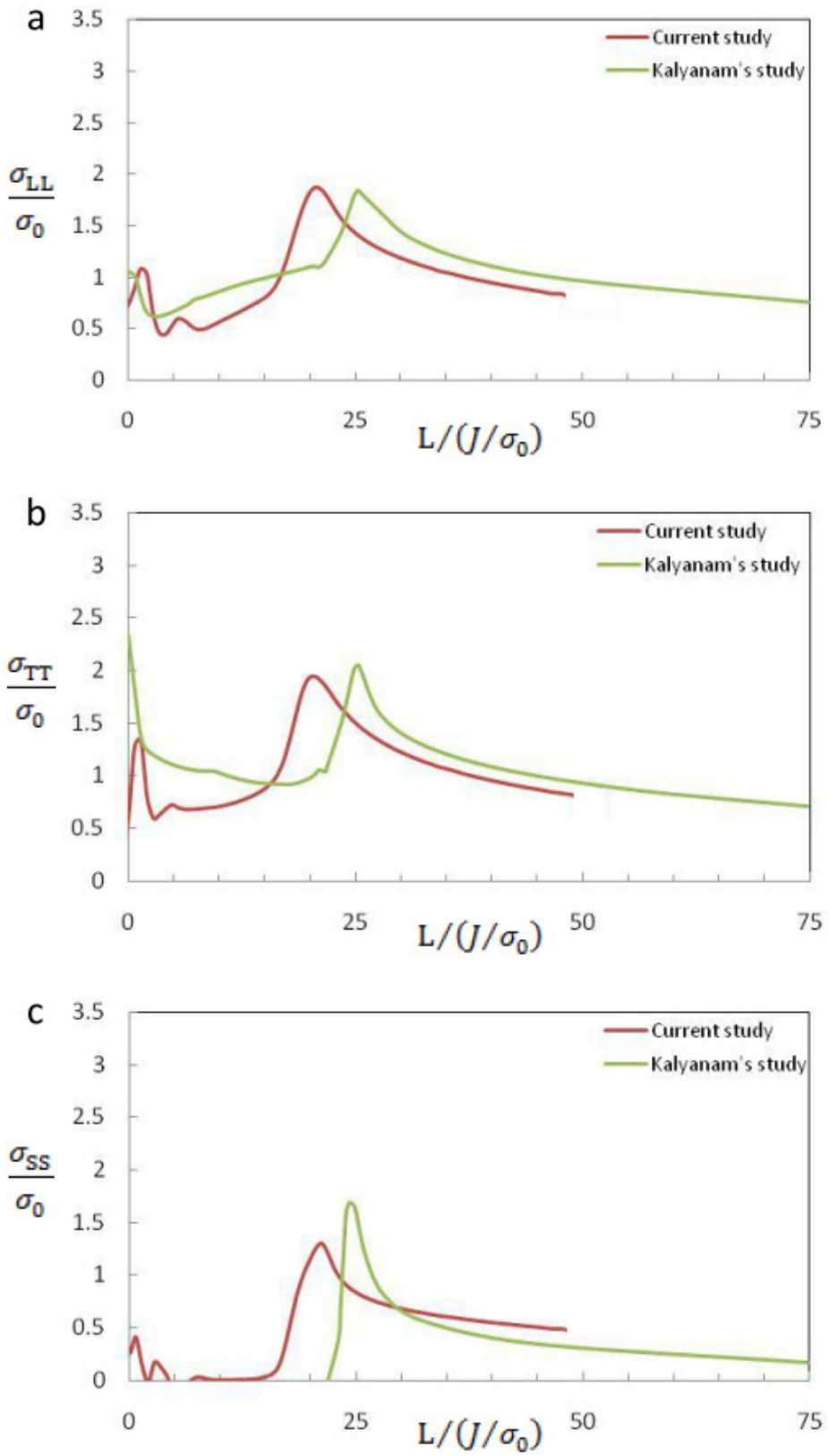

Figure 5.8: Plots comparing the stress data on the center plane ahead of the primary crack collected during the current study and presented by Kalyanam et. al. [36].

Figures 5.8a-c show the stress fields on the center plane ahead of the primary crack. The distances ahead of the crack tip are normalized by J/σ_0 [37, 38]. This scaling is similar to the HRR solution that establishes J as a stress amplitude parameter within the plastic zone. The J-value used in these normalizations comes from the K_I (with $J = K_I^2/E$) displacement field applied remotely on the boundary of the SSY model. It is clear from the figures that there is a close agreement in trends between the two sets of data. The differences between the position of the peak stress values on the normalized L-axis are attributed to the gradient of damage across the crack fronts. A result of dynamically simulating both cracks, this gradient makes it hard to pinpoint the actual edge of the cracks. The magnitudes of the peak stresses however, are in very close agreement. The differences between these peak stresses are 1.3%, 5.1%, and 26.2% for σ_{LL}, σ_{TT}, and σ_{SS} respectively. This is a very encouraging result, showing that the model used in the current study can simulate with some accuracy the stress states around the crack fronts. As a side note, the σ_{SS} stress component, which has the largest difference, is the primary driving stress for delaminations and is sensitive to texture. This study takes into account the interactions between two grains, which can significantly impact the stresses at their interface. This fact emphasizes the importance of this study and justifies its extra level of sophistication.

The effect of toughness on the failure stress of a material is a fundamental concept. Typically increasing toughness increases failure stress as illustrated in figure 5.9 above. For low toughness values there is a linear relationship, which indicates of brittle behavior. As material toughness increases the behavior moves into the plastic regime [11]. It is therefore expected that at consistent load levels, increased fracture toughness will show less crack growth.

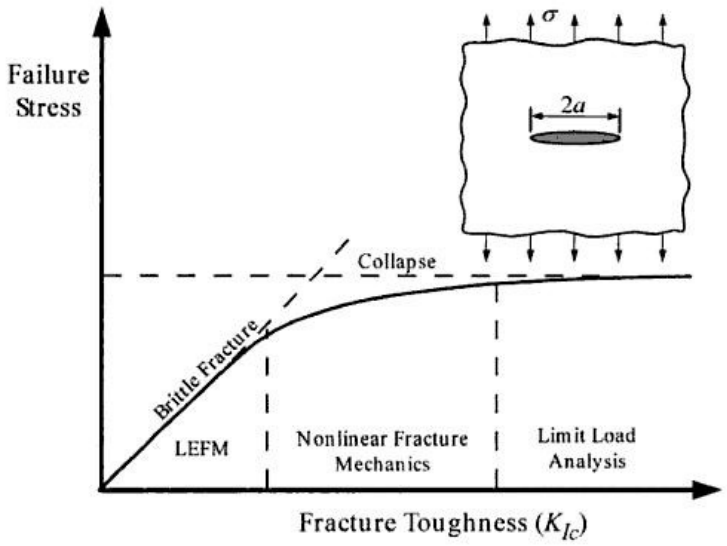

Figure 5.9: Effect of fracture toughness on the governing failure mechanism [11].

To change the material's toughness in the simulations, only manipulation of the area under the traction-separation plot was required. Recalling Eq. 3.9 and 3.10, the area under the traction-separation plot is equal to the critical energy release rate G_c. The only requirements of the manipulation were: (1) the critical tractions ($\mathcal{T}_c$) for both zones were to be maintained and (2) the ratio $\delta_c/\delta_{soft} = 20$ for each zone was also to be maintained. Taking advantage of the simple shape of the bi-linear cohesive law as well as theory from fracture mechanics [9], G_c can be expressed as

$$G_c = \frac{1}{2}\mathcal{T}_c\delta_c = \frac{K_c^2}{E} \quad . \tag{5.3}$$

Solving Eq. 5.3 for δ_c with $\mathcal{T}_c = 2\sigma_0$ yields

$$\delta_c = \frac{K_c^2}{\sigma_0 E} \quad , \tag{5.4}$$

where E is Young's modulus (78 GPa for Aluminum at room temperature). Figures 5.10a-b show the primary crack and delamination fronts at a load level of $J = 28.87$ kJ/m^2. The figures clearly show the hypothesized behavior; increases in material toughness decrease the amount of crack extension. All crack front lengths are reported at their peak locations.

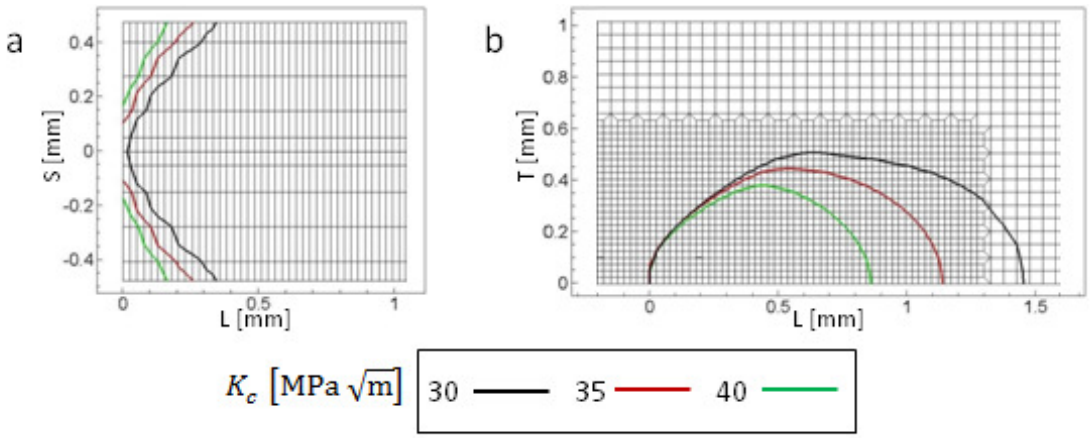

Figure 5.10: Plots showing (a) the primary crack front and (b) the delamination front for simulations using three different toughness values. All results are at an applied load of $J = 28.87$ kJ/m^2.

5.4 Effects of Crystallographic Orientations

For this portion of the study simulations were run using material parameters typical of Al-Li alloy at room temperature (see table 5.1) and varying combinations of crystallographic orientations for either side of the bi-crystal model. The six different pairs utilized (refer to table 5.2 for the angle definitions) were: cube-cube, cube-brass_1, cube-brass_2, cube-S, S-brass_1, and finally S-brass_2. To characterize the growth of the delaminations, a plot of applied load versus crack extension is shown in figure 5.11. It is evident in the figure just which pairs promote delaminations, and which have the highest resistance. The pair that initiates delamination at the lowest load is the cube-cube orientation, which is the closest orientation to isotropic and the softest. The pair that resists delamination the best is the S-brass_2 pair which may indicate that it is the hardest of the orientation pairs simulated.

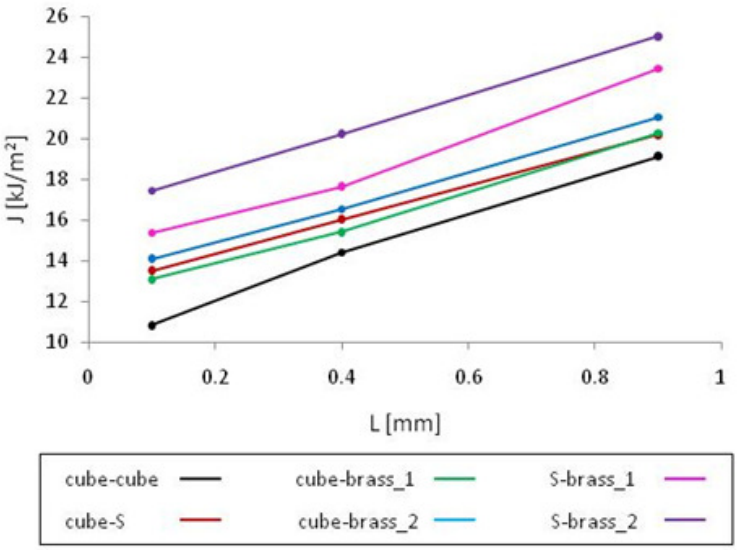

Figure 5.11: Plot of applied load versus position of the delamination leading edge along the L-axis.

For further illustration of the crack growth behavior, figures 5.12a-f show the delamination and primary crack profiles at applied loads of 15.8, 18.5, and 23.4 kJ/m^2. As discussed previously the delaminations tend to initiate in a specified order, but as seen in figures 5.12a-c, the two S-brass pairs quickly catch the other pairs, in terms of delamination extension. This behavior suggests that these pairs resist delamination better than the others, but once initiated the growth rate is higher than the other orientation pairs.

The primary crack front plots (figures 5.12d-f) shed some light on some even more interesting behavior from the S-brass pairs. First, the brass_1 grain of the S-brass_1 pair initiates primary crack growth well in advance of the S grain. Second, notice that even though the S-brass_2 pair initiates primary crack growth last, after only 5 load steps the primary crack in the brass_2 grain has far surpassed the other orientations in primary crack extension. Both of these observations suggest that there may be some interaction between grains affecting the growth of cracks both before and after a delamination has developed. That is, a stress state arising from conditions with and without some free surface on the grain boundary (a delamination) may be accentuated by the local anisotropy. These are very interesting behaviors and warrant further study.

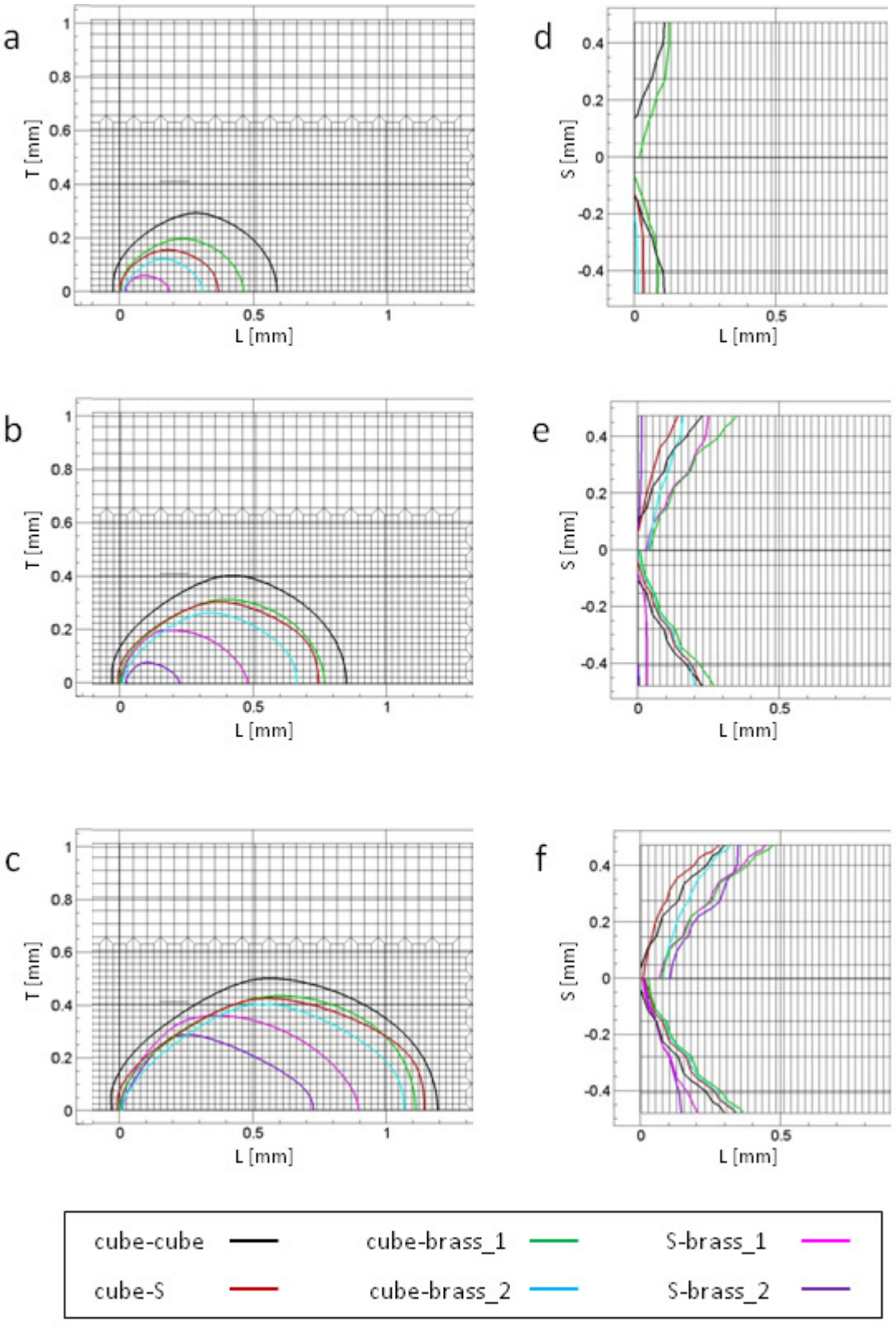

Figure 5.12: Delamination (a-c) fronts and Primary crack (d-f) fronts for all orientation pairs at applied loads: 15.8, 18.5, and 23.4. kJ/m^2 respectively.

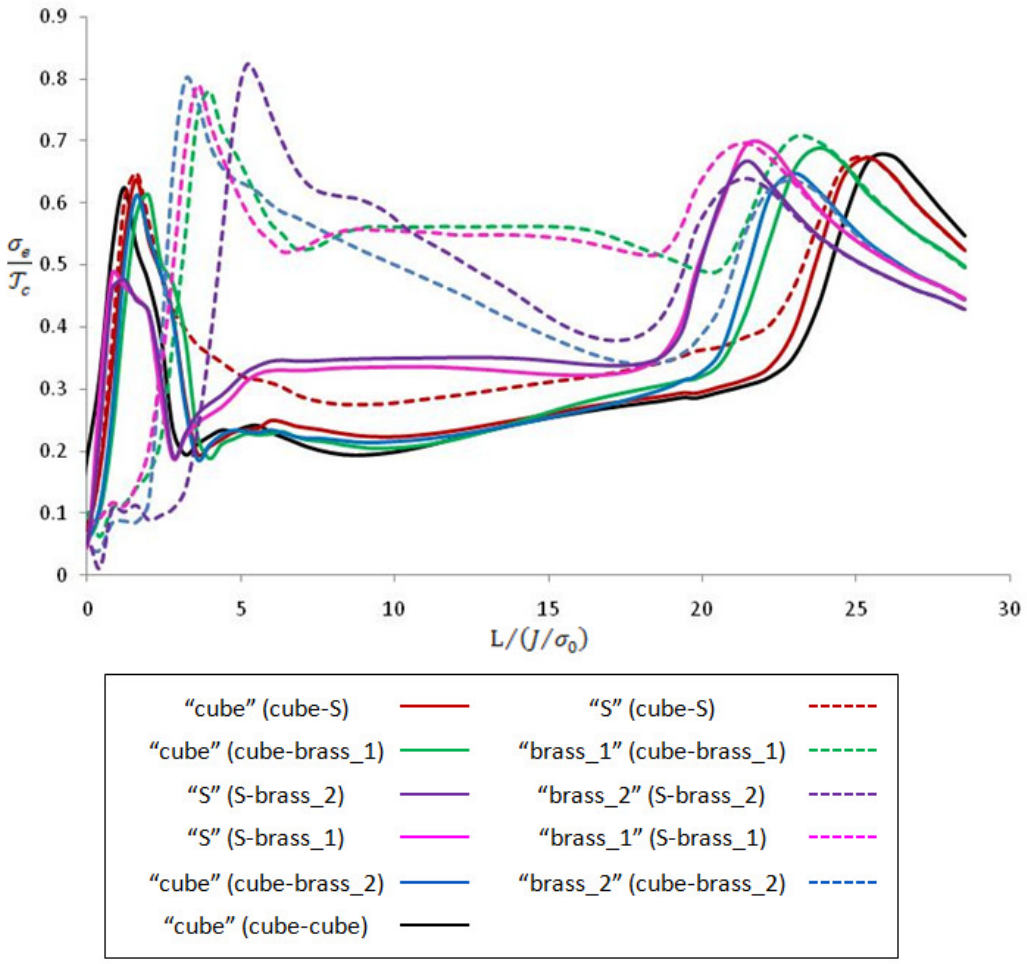

Figure 5.13: Normalized effective stress at the center of the primary crack plane at an applied load of $J = 28.87$ kJ/m^2 for various bi-crystal pairs.

To get a better handle on whether or not one orientation may be harder than the other, a plot of normalized effective stress versus normalized position along the L-axis can be examined. At an applied load of $J = 28.87$ kJ/m^2, this plot (figure 5.13) clearly shows groupings of orientations. The cube orientation is closest to isotropic, and considered to be the softest. Therefore it makes sense that all the cube grains are grouped at the lowest stress value. The brass_1 grains are grouped at the highest load level, which suggests that they may be the hardest of the orientations. The brass_2 grains show a peak value just ahead of the primary crack and a monotonic decrease until it reaches the leading edge of the delamination. This behavior again suggests that there may be some grain interactions at work, or perhaps it indicates a possible evolution of orientation that affects the grains ability to sustain load.

6 Conclusion and Recommendations for Future Work

The recent advances in the development of Al-Li alloys for aerospace applications have created a variety of different processing procedures that produce highly textured alloys with a wide range fracture toughness values. Forming a better understanding of how texture and toughness affect the delamination process was the motivation for this study. The modeling framework adopted for this study (described in some detail in chapters 2-4), allowed for simulation of the grain interactions as well as the initiation and subsequent growth of both primary cracks and delaminations. The primary results of these parametric studies and recommendations for future work are detailed in the following subsections.

6.1 Conclusions

Results from the parametric studies conducted support the following conclusions:

(1) The model used in the current study can simulate with sufficient accuracy the stress fields around the primary crack and delamination.

(2) Delaminations grow at lower loads as compared to the primary crack, suggesting that even though the applied load is Mode I for the primary crack, the complex state of stress developed ahead of the primary crack tip creates stresses at levels that easily nucleate delaminations. This observation also verifies that the strength of the grain boundary interfaces are weak in comparison to the bulk material, especially in shear.

(3) Once the initiation of a delamination occurs, an effective stress on the order of $0.9\mathcal{T}_c$ develops ahead of the delamination front indicating a self-generating localized stress field. This field has the potential to promote further extension of existing crack divider delaminations.

(4) The delamination effectively splits the primary crack and relieves the through thickness stress creating a plane stress condition at the newly formed free

surfaces. This significantly attenuates the primary crack driving force on the center plane and, as a consequence, slows the rate of its extension.

(5) The effect of toughness on a materials fracture response is well documented and is considered a fundamental concept in the study of mechanics. Therefore the result of the parametric study on fracture toughness was primarily used as a model validation and clearly indicates that an increase in fracture toughness decreases the amount of crack extension in both the primary crack and delamination.

(6) Texturing due to mechanical processing affects the magnitude of the resolved shear stress on a slip system effectively making one orientation harder than the other which dictates an orientation's resistance to fracture. The data presented in this study clearly indicates that the brass orientations are the hardest, where as the cube orientation is the softest.

(7) Observation of the differences between the stress fields and crack growth behavior of different crystallographic orientations suggests some interaction between grains affecting the growth of the cracks either before or after the delamination has developed.

6.2 Recommendations for Future Work

Based on extensive EBSD measurements of Al-Li alloy 2090 made by Wes Tayon, a grain does not consist of just one orientation. In fact near grain boundaries the orientation shows slight changes. Therefore to increase the accuracy of the model a gradient of orientations could be inputted. The results of such as study may show greater agreement with experimental measurements.

Looking back at figures 5.6a-c, it was noticed that if the J values were scaled by ~ 0.65 the data could be brought into greater agreement with Kalyanam's data. This gives rise to the question whether or not it is possible to scale isotropic data to gain insight into varying degrees of anisotropy in aluminum-lithium alloys or vice versa. It may be an interesting exercise to explore this scaling and see if there are any discernable trends.

When choosing orientation pairs for this work, a careful study was conducted to find those pairs with a high probability for delamination failure (see chapter 1). While the pairs simulated in this work do fit this criterion, there were some that had to be left out due to divergence of the material model. For example, studies conducted by Tayon show that the texture of Alloy 2090 is dominated by the brass component and that adjacent grains with differing brass variants had a high incidence of delamination failure [15]. Attempts at simulating these orientation pairs were unsuccessful. It has been suggested that the employment of the Newton-Raphson method along with the highly non-linear nature of brass-brass pairs creates a very small window of convergence. It is therefore recommended that an automatic time cutting algorithm be implemented into the code that will offer better control over convergence.

List of References

[1] Rao, K.T., Ritchie, R.O., "Fatigue of Aluminum-Lithium Alloys." *International Materials Reviews*, Vol. 37(4), pp. 153-185, 1992.

[2] Chen, P.S., Kuruvilla, A.K., Malone, T. W., and Stanton, W. P., "The Effects of Artificial Aging on the Microstructure and Fracture Toughness of Al-Cu-Li Alloy 2195." *Journal of Materials Engineering and Performance*, Vol. 7(5), pp. 682-690, 1998.

[3] McDonald, R.J., "Characterization of Delamination in 2099-T861 Aluminum-Lithium," PhD Dissertation, UIUC, 2009.

[4] Vander Kooi, D.C., Park W., and Hilton, M.R., "Characterization of Cryogenic Mechanical Properties of Aluminum-Lithium Alloy C-458." *Scripta Materialia*, Vol. 41(11), pp. 1185-1190, 1999.

[5] Hernquist, M.W., "Effects of Crack Arresting Delaminations in Aluminum-Lithium Alloys." Master's Thesis, UIUC, 2010.

[6] Srivatsan, T.S., Coyne, E.J., "Cyclic Stress Response and Deformation Behaviour of Precipitation-Hardening Aluminum-Lithium Alloys." *International Journal of Fatigue*, Vol. 8(4), pp. 201-208, 1986.

[7] Yiwen Mou, Howe, J.M., and Starke, E.A., "Grain-Boundary Precipitation and Fracture Behavior of an Al-Cu-Li-Mg-Ag Alloy." *Metallurgical and Materials Transactions A*, Vol. 26A, pp. 1591-1595, 1995.

[8] Suresh, S., Vasudevan, A.K., Tosten, M., and Howell, P.R., "Microscopic and Macroscopic Aspects of Fracture in Lithium-Containing Aluminum Alloys." *Acta Metall.*, Vol. 35(1), pp. 25-46, 1987.

[9] Miller, W.S., Thomas, M.P., Lloyd, D.J., and Creber, D., "Deformation and Fracture in Al-Li-Based Alloys." *Materials Science and Technology*, Vol. 2, pp. 1210-1216, 1986.

[10] Krüger, R. and König, M., "Prediction of Delamination Growth Under Cyclic Loading," *Composite Materials: Fatigue and Fracture STP 1285*, Vol. 6, pp. 162-178, 1997.

[11] Anderson, T.L., *Fracture Mechanics*, 3rd ed. Boca Raton: CRC Press, 2005.

[12] Sitzman, S., "Introduction to EBSD Analysis of Micro- to Nanoscale Microstructures in Metals and Ceramics." *Proceedings of SPIE*, Vol. 5392, pp. 78-90, 2004.

[13] Swapp, Susan. "Electron Backscatter Diffraction (EBSD)." SERC. Sept. 2009. Web. <http://serc.carleton.edu/research_education/geochemsheets/ebsd.html>.

[14] Yoder, G. R., Pao, P. S., Imam, M. A., and Cooley, L. A., "Prediction of Slip-Band Facet Angle in the Fatigue Crack Growth of an AL-Li Alloy" *Scripta Metallurgica*, Vol. 22, pp. 1241-1244, 1988.

[15] Tayon, W., Crooks, R., Domack, M., Wagner, J., and Elmustafa, A., "EBSD Study of Delamination Fracture in Al-Li Alloy 2090." *Experimental Mechanics*, Vol. 50, pp. 135-143, 2010.

[16] Varadhan, S., "Modeling Collective Behavior of Dislocations in Crystalline Materials." PhD Dissertation, UIUC, 2007.

[17] Follansbee, P.S., Kocks, U.F., "A Constitutive Description of the Deformation of Copper Based on the use of the Mechanical Threshold Stress as an Internal State Variable." *Acta Metall*., Vol. 36(1), pp. 81-93, 1988.

[18] Kok S., "Kinetics of Plastic Flow in Polycrystal Plasticity." PhD Dissertation, UIUC, 2002.

[19] Bonet, J. and Wood, R.D., *Nonlinear Continuum Mechanics for Finite Element Analysis*, New York: Cambridge Press, 1997.

[20] Asaro, R.J., "Crystal Plasticity." *Journal of Applied Mechanics*, Vol. 50, pp. 921-934, 1983.

[21] Hutchinson, J.W., "Bounds and Self-Consistent Estimates for Creep of Polycrystalline Materials." *Proceedings of the Royal Society of London. Series A. Mathematical and Physical Sciences*, Vol. 348, pp. 101-127, 1976.

[22] Varshni, Y.P., "Temperature Dependence of the Elastic Constants." *Physical Review B*, Vol. 2(10), pp. 3952-3958, 1970.

[23] Dugdale, D.S., "Yielding of Steel Sheets Containing Slits." *Journal of Mechanics and Physics of Solids*, Vol. 8, pp. 100-104, 1960.

[24] Barenblatt, G.I., "The Mathematical Theory of Equilibrium of Cracks in Brittle Fracture." *Advances in Applied Mechanics*, Vol. 7, pp. 55-129, 1962.

[25] Geubelle, P.H. and Baylor, J.S., "Impact-Induced Delamination of Composites: a 2D Simulation." *Composites Part B*, Vol. 29, pp. 589-602, 1998.

[26] Camacho, G.T. and Ortiz, M., "Computational Modelling of Impact Damage in Brittle Materials." *International Journal of Solid Structures*, Vol. 33) pp. 2899-2938, 1996.

[27] Xu, X. and Needleman, A., "Numerical Simulations of Dynamic Crack Growth Along an Interface." *International Journal of Fracture*, Vol. 74, pp. 289-324, 1996.

[28] Baylor, J.S., "A Numerical Simulation of Impact-Induced Damage of Composite Materials." Master's Thesis, UIUC, 1995.

[29] Klein, P.A., Foulk, J.W., Chen, E.P., Wimmer, S.A., and Gao, H.J., "Physics-Based Modeling of Brittle Fracture: Cohesive Formulations and the Application of Meshfree Methods." *Theoretical and Applied Fracture Mechanics*, Vol. 37, pp. 99-166, 2001.

[30] Papoulia, K.D., Sam, C., and Vavasis, S.A., "Time Continuity in Cohesive Finite Element Modeling." *International Journal for Numerical Methods and Engineering*, Vol. 58, pp. 679-701, 2003.

[31] Mach, J.C., "Numerical Simulation of Dynamic Strain Ageing and Fracture in Aluminum." Master's Thesis, UIUC, 2002.

[32] Ortiz, M. and Pandolfi, A., "Finite-Deformation Irreversible Cohesive Elements for Three-Dimensional Crack-Propagation Analysis." *International Journal for Numerical Methods in Engineering*. Vol. 44, pp. 1267-1282, 1999.

[33] Sam, C., Papoulia, K.D., and Vavasis, S.A., "Obtaining Initially Rigid Cohesive Finite Element Models that are Temporally Convergent." *Engineering Fracture Mechanics*, Vol. 72, pp. 2247-2267, 2005.

[34] Kocks, U. F., Tomé C. N., and Wenk, H. R., *Texture and Anisotropy*, Cambridge: Cambridge University Press, 1998.

[35] McDonald, Russell (University of Illinois at Urbana-Champaign, Dept. of Mechanical Science and Engineering, Illinois) Personal Communication, 2010.

[36] Kalyanam, S., Beaudoin, A.J., Dodds, R.H., and Barlat, F., "Delamination Cracking in Advanced Aluminum-Lithium Alloys – Experimental and Computational Studies." *Engineering Fracture Mechanics*, Vol. 76, pp. 2174-2191, 2009.

[37] Rice, J.R. and Rosengren, G.F., "Plane Strain Deformation Near a Crack Tip in a Power-Law Hardening Material." *Journal of Mechanics and Physics of Solids*, Vol. 16, pp. 1-12, 1968.

[38] Hutchinson, J.W., "Singular Behaviour at the End of a Tensile Crack in a Hardening Material." *Journal of Mechanics and Physics of Solids*, Vol. 16, pp. 13-31, 1968.